Numerical modeling of hydraulic stimulation at a fractured geothermal reservoir

균열 지열저류층에서의 수리자극 시험 수리·역학적 모델링

2018 년 2 월

서울대학교 대학원

에너지시스템공학부

유 화 정

Numerical modeling of hydraulic stimulation at a fractured geothermal reservoir

지도 교수 민 기 복

이 논문을 공학석사 학위논문으로 제출함
2017 년 12 월

서울대학교 대학원
에너지시스템공학부
유 화 정

유화정의 공학석사 학위논문을 인준함
2018 년 1 월

위 원 장 _____전 석 원_____ (인)

부위원장 _____민 기 복_____ (인)

위   원 _____송 재 준_____ (인)

Abstract

Numerical modeling of hydraulic stimulation at a fractured geothermal reservoir

Hwajung Yoo

The Graduate School

Department of Energy Systems Engineering

Rock Mechanics & Rock Engineering Laboratory

Seoul National University

Hydraulic stimulation in Enhanced Geothermal System (EGS) is prerequisite for permeability enhancements of reservoirs of which the natural permeability is low to become at commercial interests. Hydraulic stimulation is conducted by injecting a large amount of water into the reservoir at high pressure. In fractured geothermal reservoirs, hydraulic shearing on pre-existing fractures is a key mechanism to achieve permeability increases due to the dilation on the fracture planes. Hydraulic shearing is regarded as an optimal way to make irreversible permeability enhancement. Stress dependent permeability of fracture zones should be also considered as an important hydro-mechanical process.

In this thesis, wellhead pressure−versus−time curves from the field test are reproduced using TOUGH−FLAC simulator for the first two days of each hydraulic stimulation in PX−1 and PX−2 in a crystalline fractured geothermal reservoir in Pohang, South Korea. Hydro−mechanical behaviors such as hydraulic shearing and jacking in PX−1 and hydraulic jacking in PX−2 are simulated by assuming a single fracture zone model.

In the modeling of PX−1, two cases of hydraulic properties are applied to capture a pressure drop by shear at the first stage and pressure maintained pressure after shut−in at the third stage on the first day. Permanent permeability increase by shear is estimated to be hundreds times occurring up to 68−110 m from PX−1 for the two days. In the PX−2 model, simulated pressure is generally in good agreement with measured pressure for the whole period. A permeability increase to $10^{-15}\,\mathrm{m}^2$ happened to maximum 15 m from PX−2 during the two days of stimulation. This study validates the stimulation mechanisms estimated in the observational study as the first numerical stimulation study of Pohang EGS site.

A preliminary study to estimate the optimized fracture permeability and production temperature is accompanied on the assumption that injection of water at temperature of 60 ℃ at 40 kg/s for 30 years through PX−1 and PX−2. With fracture permeability in the range of $6.74{\times}10^{-13}\,\mathrm{m}^2 \sim 6.74{\times}10^{-12}\,\mathrm{m}^2$, pressure demands on

pumps smaller than 35 MPa are predicted from the simulation.

Contents

Lists of tables

Lists of Figures

Chapter 1. **Introduction**

1.1 Hydraulic stimulation in EGS

Enhanced Geothermal Systems (EGS), previously named Hot Dry Rock (HDR), are defined as geothermal reservoirs that have been created to extract economical amounts of heat from low permeability geothermal reservoirs. As shown in Figure 1.1, thermal energy is extracted from the rocks by injecting water at lower temperature to injection wells, circulating it through the reservoir, and producing hot water or steam from production wells. Commercial energy product such as electricity and heat is generated from the produced hot water or steam. The technically feasible depth for rock to circulate water is in the range of 3 to 5 km (Tester et al. 2006).

EGS requires artificial processes for permeability enhancement as the natural permeability of the reservoir is too low to be commercially feasible. In the natural reservoirs, the fluid may be depleted during production due to the low permeability, which may be caused by lack of fractures or poor hydraulic connection in fracture network systems. The low hydraulic conductivity restricts the area for the geothermal heat exploitation (Genter et al. 2010; Sanyal et al. 2000).

The artificial processes to increase permeability of EGS

reservoirs are called stimulations. General methods for stimulation are hydraulic, chemical and thermal stimulations. Hydraulic stimulation is a technique to improve permeability by injecting a large volume of fluid to the reservoir at high pressure. A successful hydraulic stimulation allows fluid to circulate between the injection and production wells at commercially feasible flow rate (Genter et al. 2010).
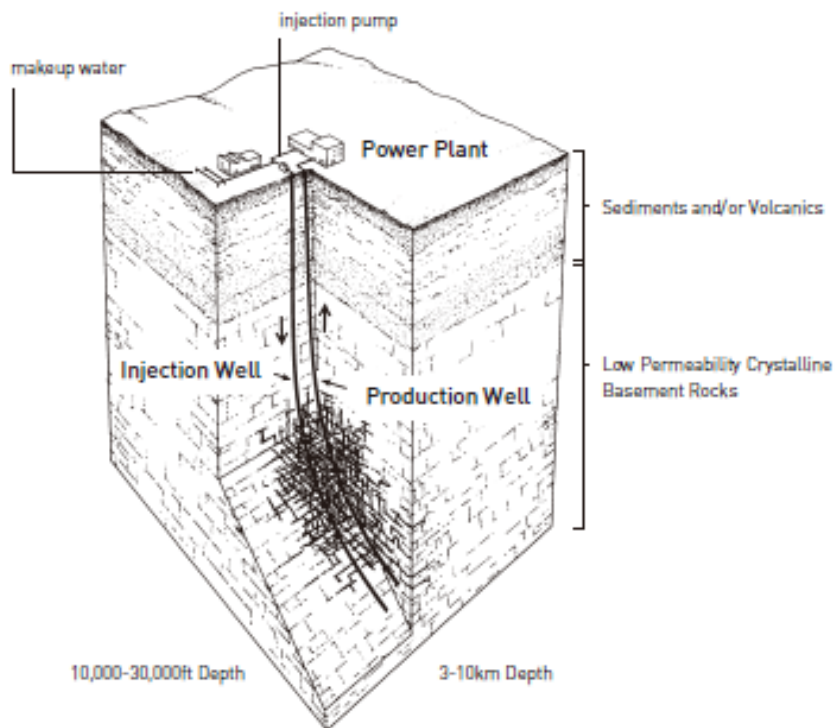
Figure 1.1: Conceptual diagram of an Enhanced Geothermal System (EGS) (Tester et al. 2006).

2

Hydraulic stimulation has been essentially required to enhance permeability in EGS reservoirs. Xie et al. (2015) reported that there had been almost ten EGS or HDR projects that had been or was being developed and tested in the world: Fenton Hill in the USA, Rosemanowes in the UK, Soultz in France, Ogachi in Japan, Hijiori in Japan, Cooper Basin in Australia, Gross Schonebeck in Germany, and Basel in Switzerland.

In fractured rock reservoir, preexisting fractures can be potential flow paths that connect injection and production wells. Reactivation of such preexisting fractures by shearing is a key process to improve the permeability permanently due to the dilation of fractures. Hydraulic fracturing is another way to make flow paths by creating new tensile fractures (Xie et al. 2015). Non-linear changes in equivalent apertures over effective normal stress on fractures also have to be considered essential in fractured media (Min et al. 2004; Rutqvist and Tsang 2003). In order to analyze a hydraulic stimulation in an EGS reservoir, these hydromechanical behaviors has to be understood comprehensively.

1.2 Production estimation of in EGS

Sustainable production in the long term is a critical issue that decides the lifespan of an EGS reservoir. It is essential to maximize the heat extraction from the reservoir and to maintain the heat extraction rate for the operation period. The amount of heat extraction is proportional to the mass flow rate and production temperature.

The pressure at wells and flow rate interact each other; for a higher flow rate, a higher pressure drop at the production well and a higher pressure increase at the injection well accompanies. The permeability of the reservoir and the pathway of the circulation fluid decide a natural flow rate and the corresponding pressure changes at the wells. Higher permeability and shorter pathway lowers pressure changes and reduce the work of pumps. Buoyancy effects due to the density difference by temperature leads self-pumping, decreasing the pump-work. For instance, the pressure change at well by buoyancy could be around 10 MPa for a 250 ℃ reservoir at 6 km. In order to minimize the pump work, the reservoir permeability should be high enough and the pathway between the wells be not too long (Tester et al. 2006).

Temperature drawdown of produced fluid determines a sustainable exploitation of heat. The heat in the reservoir should be

extracted efficiently for the whole operation, and some temperature should be kept in the consideration of heat recovery and future heat mining (Tester et al. 2006). Beardsmore et al. (2010) suggested an allowable drawdown of less than 10 °C for 30 years of operation. The larger the area heat is transferred from is and the smaller the flow rate is, the less thermal drawdown is. In fractured geothermal reservoirs, the area and distribution of fractures are the parameters that primarily affect the thermal performance (Armstead and Tester 1986; Bodvarsson 1969; Gringarten et al. 1975).

It is required to estimate and evaluate production rate and temperature for the production ahead of an EGS operation. Optimized distance between wells can be estimated and help to decide drilling locations. In addition, it can be estimated to what extent the reservoir permeability has to be enhanced by stimulation.

1.3 Objectives and Motivations

Hydromechanical numerical modeling of hydraulic stimulations can help to improve the understanding on an EGS reservoir. Numerical modeling can be used to reproduce field data such as pressure curves and microseismic events. The simulation ultimately helps to understand permeability changes during the stimulation and estimate possible permeability enhancement in the geothermal reservoir. The simulation results are sources to validate the conceptualized reservoir model by comparing them with field data. In addition, the values of uncertain hydraulic and mechanical properties, especially properties on the fracture, can be estimated during the calibration process. For those purposes, hydraulic stimulation has been numerically modeled for other EGS sites, e.g., Desert Peak in the US (Dempsey et al. 2015), the Geysers in the US (Jeanne et al. 2015), Soultz-sous-Forets in France (Tenzer et al. 2010; Wassing et al. 2014) and Spa Urach in Germany (Tenzer et al. 2010).

Estimation of production rate and temperature should precede an actual operation. There have been developments of analytical solutions to calculate reservoir and production temperature during circulation using simplified conceptual models of fracture arrangements or reservoir shapes, e.g., a single rectilinear fracture (Bodvarsson 1969), multiple parallel rectilinear fractures with

uniform spacing (Gringarten et al. 1975), multiple parallel radial fractures with uniform spacing (Bödvarsson and Tsang 1982), spherically stimulated reservoir model (Elsworth 1989). Complementing limitation of analytic analyses that only simple geometry is available, numerical modeling have been studied and conducted by many researchers, e.g. Willis–Richards and Wallroth (1995), Kolditz and Clauser (1998), Blöcher et al. (2010), Shaik et al. (2011), Wong et al. (2012) and Zeng et al. (2013).

The first EGS project started in 2010 in Pohang, South Korea. The project aimed to achieve 1 MW scale geothermal power generation in a doublet system. The first hydraulic stimulation was conducted in PX–1 and PX–2 well between January 2016 and December 2016. Park et al. (2018b) analyzed the stimulation results and mechanisms for stimulation based on field observation.

In the current thesis, numerical simulation of the hydraulic stimulation in PX–1 and PX–2 well and for a long–term production estimation is conducted. In the simulation of hydraulic stimulation part, it aims to capture hydromechanical behaviors in the fractured porous EGS reservoir during the hydraulic stimulation and to estimate the permeability enhancement in PX–1 and PX–2. For that, pressure curves from the field experiment is numerically reproduced. Followed by the simulation of hydraulic stimulation, a preliminary study is conducted to estimate temperature and required permeability for a target production rate and temperature in Pohang

EGS reservoir. Hydrothermal behavior is simulated in this part. This thesis has a significance as the first numerical modeling of Pohang EGS site.

Chapter 2. **Background and theory**

2.1 Hydraulic stimulation in Pohang EGS site

2.1.1 Overview of the site

The first EGS development project in Korea started in Pohang, located at the south—eastern part of Korea, at 36°06'24"N 129°22'42"E, at the end of 2010. The reservoir is fractured porous media consisting of granodiorite down below the depth of 2.4 km. The granodiorite reservoir is covered by a sequence of andesites and crystal tuffs, a 1 km thick Cretaceous sedimentary layer of sandstones and mudstones, and a 200 to 400 m Teritiary semi—consolidate mudstone from a deeper to swallower depth (Lee et al. 2015).
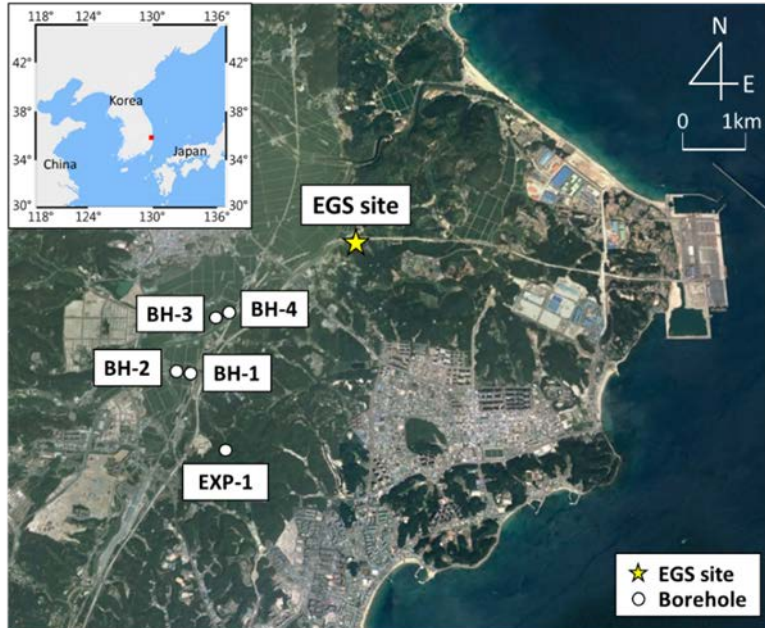
Figure 2.1: Locations of the Pohang EGS site and the five wells near the site (Kim et al. 2017b).

Two boreholes, PX−1 and PX−2 are drilled in the EGS site, and 5 wells, BH−1~BH−4 and EXP−1, are located within 5 km from the site. PX−1 is a deviated well, and drilled up to 4,362 m as measured depth and 4,217 m as true vertical depth. PX−1 has 313 m of openhole section from 4,049 m to 4,362 m as measured depth, and 3,920 m to 4,217 m as true vertical depth. PX−2 is a vertical well and drilled up to 4,348 m. The openhole section of PX−2 is 140 m from 4,208m to 4,348 m both as measured and true vertical depth. The two wells are 6 m apart on the surface and about 600 m apart at the bottom hole (Park et al. 2018b).

A preexisting fracture zone dipped at 65°~70° with 20°~30° of

dip direction is presumed to intersect the openhole section of PX-1 and PX-2 (Figure 2.1). The existence of the fracture zone was inferred based on magnetotelluric survey in Pohang (Lee et al. 2015), massive lost circulations during the drilling of PX-2 and WNW-ESE lineament structures observed from the surface geology. The preexisting fracture zone is expected to be the potential main flow path (Park et al. 2018b).

In the first hydraulic stimulations in PX-1 and PX-2, various stimulation strategies were implemented such as step rate tests, cyclic injections, continuous injections, long term shut-ins, sudden high-rate injections and bleed-offs (Park et al. 2018b). A protocol for induced seismicity (Kim et al. 2017b) was applied during the hydraulic stimulation. This study focuses on the first hydraulic stimulation in PX-2 well from January 29 to February 20, 2016 and in PX-1 well from December 15 to 28, 2016.

2.1.2 Hydraulic stimulation in PX-1 well

In the first stimulation of PX-1, the net injection volume was 2,689 m^3 corresponding to 3,907 m^3 of injection volume and 1,218 m^3 of bleed-off. As shown in Figure 2.2, the maximum wellhead pressure was 27.7 MPa, and the maximum flow rate was 18.0 L/s. Clear increases in injectivity was observed at the wellhead pressure of 16 MPa. This pressure is analogous to pressure peaks that

11

appeared at 15~17 MPa on the first day. Wellhead injectivity in PX−1 ranged from 0.37 to 0.58 L/s/MPa at the injection rate of 10 L/s, which are 3.7 times higher than that in PX−2 (Park et al. 2018b).

The stimulation mechanism was estimated to be hydraulic shearing and jacking on the preexisting fracture zone. In the baseline scenario for in−situ stress suggested in Park et al. (2018b), the critical pressure for shearing was estimated to be 15 MPa. As the initial pressure peak in the PX−1 stimulation was between 15 and 17 MPa, it is highly likely that hydraulic shearing occurred. Also, jacking behavior on the fracture, fracture opening−up and closing−down, was expected to have happened in accordance with changing effective normal stress.
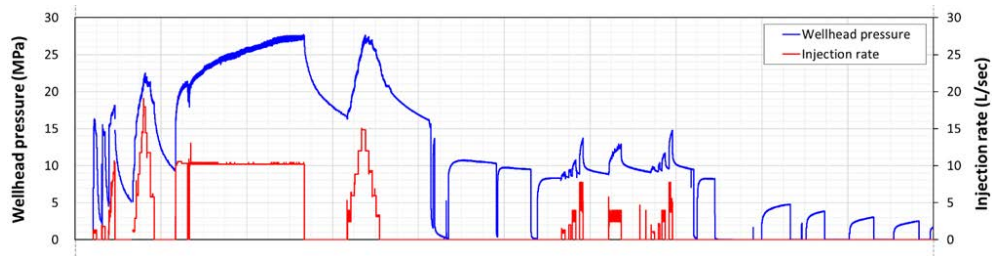
Figure 2.2: Wellhead pressure and injection rate curves of hydraulic stimulation in PX-1 from 15th to 28th of December 2016 (Park et al. 2018b)

2.1.3 Hydraulic stimulation in PX−2 well

The total injected volume of water was 1,970 m^3 in the PX−2 stimulation. The maximum wellhead pressure reached 89.2 MPa, and the maximum flow rate was 46.8 kg/s. The wellhead pressure was stabilized at the wellhead pressure of 64~67 MPa on the second day (Figure 2.3). Injectivity obviously increased at 73 MPa, which is similar to the stabilized wellhead pressure (Park et al. 2017).

Stimulation mechanism for PX−2 was estimated to be a combination of hydraulic fracturing and jacking in Park et al. (2017). Breakdown wellhead pressure for hydraulic fracturing is 72.9 MPa in the baseline scenario of the in−situ stress. The probability of the hydraulic fracturing was inferred from the reasonable agreement between the stabilized wellhead pressure and the estimated breakdown pressure. The critical jacking pressure was estimated to be 46.7 MPa, which was smaller than the stabilized wellhead pressure measured in the field. However, the discrepancy could be explained by other field experiments, and the high likelihood for jacking was acceptable (Park et al. 2018b).
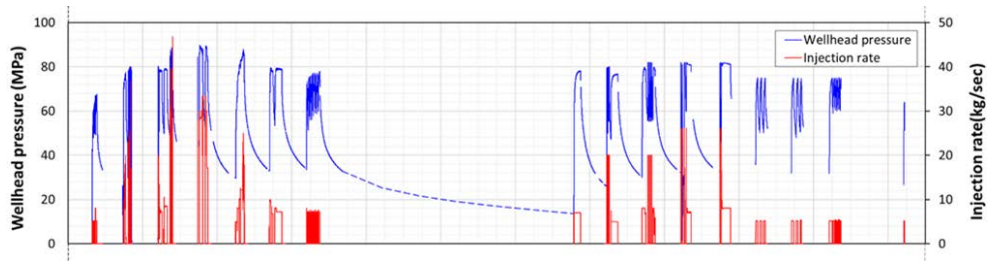
Figure 2.3: Wellhead pressure and injection rate curves of hydraulic stimulation in PX-2 from 29th of January to 20th of February 2016 (Park et al. 2017)

2.2 Numerical simulator

2.2.1 TOUGH2

TOUGH2 (Pruess et al. 2011) is a numerical simulator for hydraulic and thermal behaviors of multicomponent, multiphase fluids in porous and fractured media. Since the first release to public by Lawrence Berkeley National Laboratory in USA in 1991, TOUGH2 has been applied in geothermal reservoir engineering, nuclear waste disposal, environmental assessment and remediation, and hydrology in saturated and unsaturated media. TOUGH2 provides "EOS" (equation−of−state) modules that contain different fluid properties including water, air, CO2, brine, salt and hydrogen. Users can select modules for their purposes.

According to the manual of TOUGH2, TOUGH2 solves mass and energy balance equations written in the following form:

$$\frac{\mathrm{d}}{\mathrm{dt}} \int_{V_n} M^\kappa dV_n = \int_{\Gamma_n} \boldsymbol{F^\kappa} \cdot \boldsymbol{n} d\Gamma_n + \int_{V_n} q^\kappa dV_n \qquad (2.1)$$

The integration is over an arbitrary subdomain V_n of the flow system, which is bounded by the closed surface Γ_n. The quantity M denotes mass or energy per volume where $\kappa = 1$ to NK labels the mass components and $\kappa = NK+1$ the heat component. $\mathbf{F}$ represents mass or heat flux, and q represents sinks and sources. n is a normal vector on surface element inward into V_n.

15

The general form of the mass accumulation term is

$$M^\kappa = \phi \sum_\beta S_\beta \rho_\beta X_\beta^\kappa \qquad (2.2)$$

The total mass of component κ is obtained by summing over the fluid phases β. ϕ denotes porosity, S_β is the saturation of phase β, ρ_β is the density of phase β, and X_β^κ is the mass fraction of component κ in phase β. The heat accumulation term is written as

$$M^{NK+1} = (1 - \phi)\rho_R C_R T + \phi \sum_\rho S_\beta \rho_\beta u_\beta \qquad (2.3)$$

where σ_R and C_R are grain density and specific heat of the rock, respectively, T is temperature, and u_β is specific internal energy in phase β.

Advective mass flux is a summation over phases as below:

$$F^\kappa|_{adv} = \sum_\beta X_\beta^\kappa F_\beta \qquad (2.4)$$

Individual phase fluxes are written in a multiphase version of Darcy's law:

$$\mathbf{F}_\beta = \rho_\beta \mathbf{u}_\beta = -k \frac{k_{r\beta} \rho_\beta}{\mu_\beta} (\nabla P_\beta - \rho_\beta \mathbf{g}) \qquad (2.5)$$

where u_β is the Darcy velocity (volume flux) in phase β, k is absolute permeability, $k_{r\beta}$ is relative permeability to phase β, μ_β is viscosity, and P_β is the fluid pressure in phase β. Heat flux is composed of conductive and convective components,

$$\mathbf{F}^{NK+1} = -\lambda \nabla T + \sum_\beta h_\beta \mathbf{F}_\beta \qquad (2.6)$$

where λ is thermal conductivity, and h_β is specific enthalpy in phase β. Mass transport by diffusion and hydrodynamic dispersion is written as

$$\mathbf{F}^\kappa|_{dis} = -\sum_\beta \rho_\beta \overline{\mathbf{D}}_\beta^\kappa \nabla X_\beta^\kappa \qquad (2.7)$$

where $\overline{\mathbf{D}}_\beta^\kappa$ is hydrodynamic dispersion tensor.

The integral finite difference method is used in TOUGH2. Space is discretized using appropriate volume averages for volume integrals and a discrete sum over surface segments for surface integrals. Time is discretized as a first−order finite difference. More detailed process for the integral finite difference can be found in the TOUGH2 user's guide (Pruess et al. 2011).

2.2.2 FLAC3D

FLAC3D (Itasca 2009) is a three−dimensional explicit finite−difference program for simulating the behaviors of materials such as soil and rock that undergo plastic flow after reaching their yield limits. FLAC3D is an ideal analysis tool in geotechnical engineering. Each element behaves according to a prescribed stress/strain law in responses to applied forces or boundary restraints. The material can yield and flow, and the grid can accordingly deform and move. FLAC3D can model plastic collapse very accurately as it does not form matrices so the calculation can be made without any excessive

17

memory requirement.

FLAC3D offers thirteen basic built–in material models: the "null" model, three elasticity models (isotropic, transversely isotropic and orthotropic elasticity), and nine plasticity models (Drucker–Prager, Mohr–Coulomb, strain–hardening/softening, ubiquitous–join, bilinear strain–hardening/softening ubiquitous–joint, double–yield, modified Camclay, Cysoil, and Hoek–Brown).

In this study, the elastic, isotropic model and bilinear strain–softening ubiquitous–joint model are implemented. In the elastic, isotropic model, strain increments generate stress increments accruing to the linear and reversible law of Hooke given as

$$\Delta\sigma_{ij} = 2G\Delta\epsilon_{ij} + \alpha_2\Delta\epsilon_{kk}\delta_{ij} \tag{2.8}$$

where the Einstein summation convention applies, δ_{ij} is the Kroenecker delta symbol, and α_2 is a material constant related to the bulk modulus, K, and shear modulus, G, as

$$\alpha_2 = K - \frac{2}{3}G \tag{2.9}$$

New stress values are then obtained from the relation

$$\sigma_{ij}^N = \sigma_{ij} + \Delta\sigma_{ij} \tag{2.10}$$

In the bilinear strain–softening ubiquitous–joint model, the failure envelops for the matrix and joint are composed of two Mohr–Coulomb criteria with a tension cutoff that softens according to specified law. The failure envelop by the Mohr–Coulomb failure criterion is

$$f^s = \sigma_1 - \sigma_3 N_\phi + 2c\sqrt{N_\phi} \qquad (2.11)$$

and that by a tension failure criterion is

$$f_t = \sigma_3 - \sigma^t \qquad (2.12)$$

where ϕ is the friction angle, c is the cohesion, and σ^t is the tensile strength, and

$$N_\phi = \frac{1 + \sin(\phi)}{1 - \sin(\phi)} \qquad (2.13)$$

General failure is first detected each step, and plastic corrections are applied. Then new stresses for failure are analyzed and updated. It is assumed that the total strain increments can be decomposed into elastic and plastic parts. The flow rule for plastic yielding is in the following form

$$\Delta\epsilon_i^p = \lambda\frac{\partial g}{\partial \sigma_i} \qquad (2.14)$$

where i=1, 3. The potential function, g, is $\mathbf{g^s}$ for shear yielding and $\mathbf{g^t}$ for tensile yielding. The potential function for shear yielding is

$$g^s = \sigma_1 - \sigma_3 N_\psi \qquad (2.15)$$

where ψ is the dilation angle, and

$$N_\psi = \frac{1 + \sin(\psi)}{1 - \sin(\psi)} \qquad (2.16)$$

The potential function for tensile yielding is written as

$$g^t = \sigma_3 \qquad (2.17)$$

2.2.3 TOUGH-FLAC simulator

TOUGH-FLAC (Rutqvist 2011) is a coupled thermal-hydro-mechanical (THM) simulator in geological media, which couples TOUGH2 and FLAC3D. In TOUGH-FLAC, TOUGH2 solves multiphase flow and heat transport equations, and FLAC3D deals with geomechanical behaviors. TOUGH-FLAC has been widely applied in various underground THM problems such as nuclear waste disposal, CO_2 sequestration and geothermal energy.

Figure 2.4 presents the coupling process of TOUGH-FLAC in a THM simulation. Stress and strain are obtained in FLAC3D and transported to TOUGH2 in order to update hydraulic properties, porosity, permeability, and capillary pressure. Mechanically induced changes in porosity can be calculated by a poro-elastic model or by an empirical model as a function of effective stress. Permeability can be calculated by empirical equations selected by a user. Especially for fractured media, an exponential permeability function of effective normal stress is applicable for the hydraulic aperture of fractures.

Pressure, temperature and saturations are computed in TOUGH2, and given to FLAC3D for the estimation of effective stress, thermal stress and hydraulic or thermally induced strains. Changes in pressure, temperature and saturations may influence mechanical properties such as bulk modulus, shear modulus, cohesion, and friction coefficient.
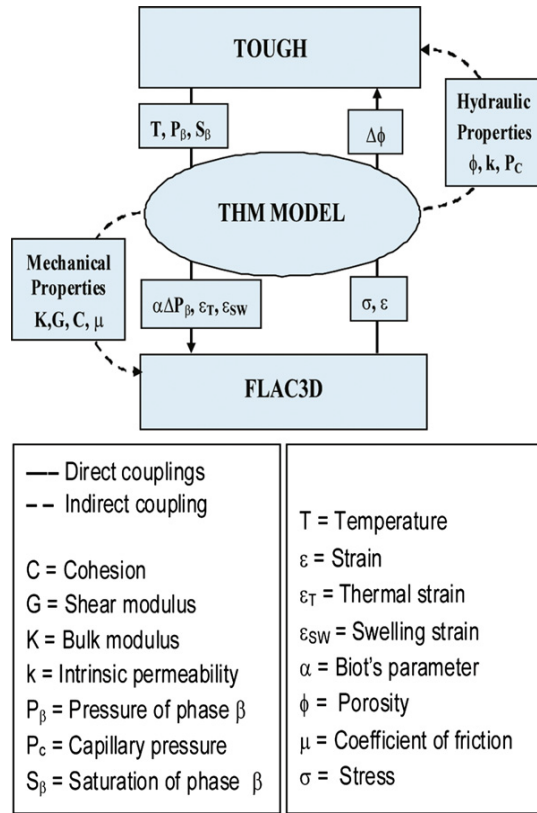
Figure 2.4: Schematic diagram of coupling of TOUGH2 and FLAC3D in TOUGH-FLAC for a coupled THM simulation (Rutqvist 2011).

Lee (2014) conducted a verification study for hydromechanical responses in TOUGH−FLAC by comparing with Terzagi's analytical solution. A mechanical loading was applied on a boundary in a one dimensional saturated poroelastic model. Transient pore pressure on the unloaded boundary and displacement on the loaded boundary were measured. The simulation results were in good agreement with the analytical solution as shown in Figure 2.5. This study verified the reliability of TOUGH−FLAC for hydromechanical coupling.
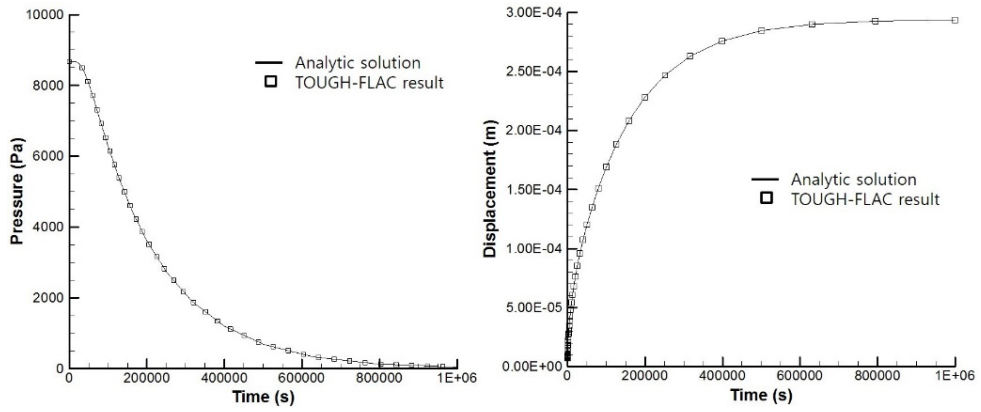
Figure 2.5: Verification of hydromechanical behaviors in TOUGH-FLAC using the uniaxial consolidation analysis (a) evolution of pressure at the unloaded boundary, (b) evolution of displacement at the upper boundary (Lee 2014)

2.3 Hydro-mechanical behavior

2.3.1 Hydraulic shearing

Hydraulic shearing on existing fractures is the main mechanism for hydraulic stimulation in EGS (Genter et al. 2010; Tester et al. 2006). Injected water increases pore pressure and decreases effective stresses, σ', which is written as

$$\sigma_1' = \sigma_1 - P, \qquad \sigma_2' = \sigma_2 - P, \qquad \sigma_3' = \sigma_3 - P \qquad (2.18)$$

where P is the pore pressure. As pressure increases, the Mohr's circle moves leftwards, and when it reaches the critical pore pressure of fracture, a shear slip occurs (Figure 2.6a). Associated shear dilations increase hydraulic aperture of the fractures.
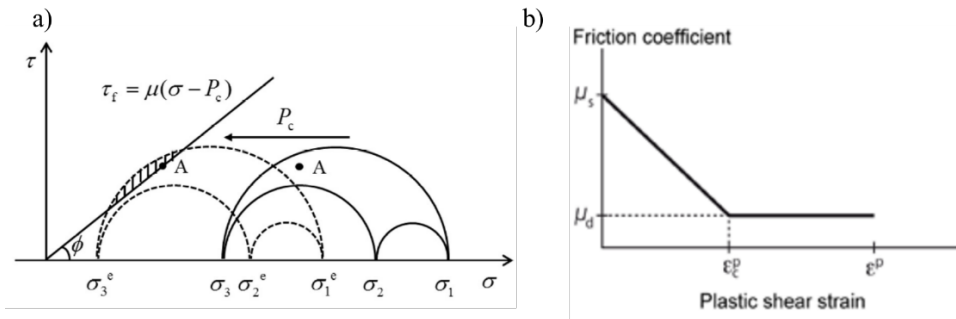
Figure 2.6: (a) Conceptual diagram of hydraulic shearing (Xie and Min 2016), (b) A plastic shear strain-weakening friction law (Cappa and Rutqvist 2011).

In this study, modeling of shearing basically followed the approach in Rinaldi and Rutqvist (2018). Occurrence of shear dilation is determined under the Mohr−Coulomb failure criterion.

$$|\tau| = \mu(\sigma - P) \tag{2.19}$$

where σ is the normal component on the fracture, τ is the shear component, and μ is friction coefficient, when fracture cohesion is regarded as zero.

Hsiung et al. (2005) derived an aperture change due to plastic deformation such as shear dilation and tensile failure in fractured rock. When one fracture set consists of the fracture zone, shear dilation is calculated by:

$$b_{shear} = L \cdot \epsilon_s \cdot tan\varphi \tag{2.20}$$

where L is thickness of a fracture zone, ϵ_s is fracture plastic shear strain, and φ is shear dilation angle of a fracture zone.

In order to describe a sudden shear slip, a strain softening joint model in FLAC3D was selected in the fracture zone by linearly decreasing friction coefficient of an element once shearing appears in the element (Figure 2.6b). The residual dynamic friction angle and the critical plastic shear strain at which the friction angle reaches the residual friction angle are parameters that affect onset and areal extent of the shearing (Rutqvist et al. 2015). The critical plastic shear strain and residual friction angle in the fracture zone could not be obtained in the laboratory test, so they were determined by calibration through a sensitivity test in this work. The maximum

24

shear dilation is applied by following equation:

$$\max(b_{shear}) = L \cdot \epsilon_c \cdot \tan\varphi \qquad (2.21)$$

where ϵ_c is the critical shear strain.

2.3.2 Stress dependent permeability

Equivalent hydraulic aperture of a fracture zone is related to an exponential function of effective normal stress as the following equation (Rutqvist and Tsang 2003):

$$b_{elastic} = b_r + b_{max} \cdot \exp(d \cdot \sigma_n') \qquad (2.22)$$

where b_r is residual hydraulic aperture, b_{max} is the maximum deformation of aperture which appears when the effective normal stress (σ_n') is zero, and d is a parameter related to the curvature of the aperture-stress curve. This equation represents a jacking behavior on the fracture zone in which the fractures open up and close down at high and low effective normal stress, respectively.

As only shearing and jacking on an existing fracture zone is taken in into account in this modeling, the hydraulic aperture in the fracture zone is calculated as the sum of shear dilation and elastic equivalent hydraulic aperture:

$$b = b_{shear} + b_{elastic}$$
$$= L \cdot \epsilon_s \cdot \tan\varphi + b_r + b_{max} \cdot \exp(d \cdot \sigma_n') \qquad (2.23)$$

As shown in Figure 2.7, hydraulic aperture of the fracture zone has elastic component initially and is the exponential function of effective

normal stress in the form of Eq. (2.22). Once it shears, it starts to follow a new aperture function increased by the shear dilation as Eq. (2.23). Permeability, k, of the single fracture zone with a thickness of L is obtained by applying the hydraulic aperture into Cubic law (Witherspoon et al. 1980):

$$k = b^3/12L \qquad (2.24)$$
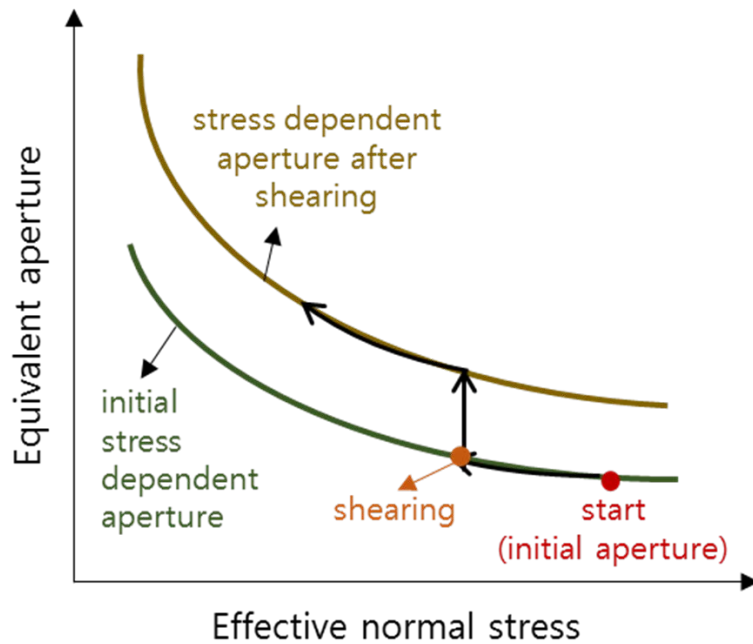
Figure 2.7: Conceptual diagram of equivalent fracture aperture describing a function of effective normal stress and an equivalent aperture increase by the shear dilation (redrawn based on Vilarrasa et al. (2017)).

2.4 Hydro-thermal behavior

2.4.1 Modeling approach

Modeling approaches for fractured geothermal reservoir can be divided into two, the explicit fracture approach and the effective continuum approach. Modeling fractures explicitly is ideal, but geometric detail is required in this approach. Considering a fractured medium as a continuum porous medium can be a solution for the problem. The continuum approach is easy to deal with, but entails a drastic simplification. The continuum approach can be justified when fracture spacing is small enough for thermodynamic equilibrium between fractures and matrix. The fracture spacing must be less than 2－3 m for thermodynamic equilibrium within a few months (Pruess 1990). According to a calculation of Armstead and Tester (1986), 26 m is the maximum fracture spacing for continuum approach for 20 years of operation in a typical granite reservoir.

In this study, we presumed a 3.3 m thickness of the fracture zone as continuum porous medium. It should be noted that this approach is valid under the assumption that the fracture zone is fractured densely enough to have thermodynamic equilibrium. Also, there is a possibility that the heat extraction in the early days could be overestimated in the modeling.

2.4.2 Verifications

A verification of heat transfer in TOUGH2 is conducted by comparing with a two−dimensional analytic solution for a rectilinear fracture model (Gringarten et al. 1975). In this solution, it is assumed that fluid is injected at constant mass rate and temperature to multiple parallel fractures with uniform spacing (Figure 2.8). When fluid moves in the x direction through fractures that are normal to the z direction, the transient rock and fluid temperature can be calculated using the following equation:

$$T_D(x_D, z_D, s) = \frac{1}{s}exp\left[-x_D\sqrt{s} * tanh(\beta D_{ED}\sqrt{s})\right] \qquad (2.25)$$
$$\cdot \left[cosh(\beta z_D\sqrt{s}) - tanh(\beta D_{ED}\sqrt{s})sinh(\beta z_D\sqrt{s})\right]$$

where T_D is the Laplace transform of dimensionless temperature, x_D and z_D are the dimensionless x and z, s is the Laplace parameter, D_{ED} is the dimensionless half−spacing, H is an arbitrary value for dimensionless forms, and β is defined as

$$\beta = \frac{c_w Q}{2kHNW} \qquad (2.26)$$

where c_w is the specific heat of fluid, Q is the total mass flow rate, k is the thermal conductivity of rock, N is the number of fractures, and W is the fracture width. The analytic solution can be solved by Laplace inversion, and we obtained the solution using a simulator made by Park et al. (2018a), which builds in the Gringarten's solution.

28
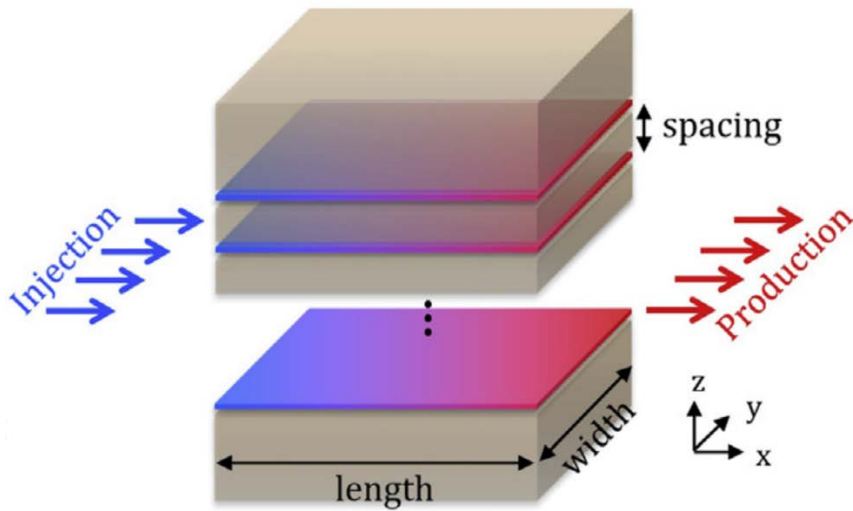
Figure 2.8: Schematic of a rectilinear fracture model used in Gringarten et al. (1975) (Park et al. 2018a).

In a 2D model, fracture elements as thin as 0.001 m is located between two impermeable rock mass zones as thick as 214 m each. The length of the fracture is 100m. The initial rock temperature is 40 °C. 20 °C water is injected at 0.01 kg/s through an end of the fracture, and hot water is produced at the other end at 0.01 kg/s (Figure 2.9). Thermal properties used in the model is shown in Table 2.1. Although specific heat of water is temperature dependent in TOUGH2, its range is not large between 20 and 40 °C. Therefore, a single value of 4178 J/kg·K is assumed in the analytic solution. Transient temperature at 9.5, 19.5, 49.5, 89.5 m from the injection point along the fracture is measured for a year. The simulated temperature is in good agreement with the analytic solution (Figure

2.10), so thermo−hydraulic response in TOUGH2 is well verified.

Table 2.1 Properties used in the verification model

Properties	Value
Specific heat of rock	920 J/kg·K
Specific heat of fluid	4178 J/kg·K
Rock density	2500 kg/m^3
Thermal conductivity of rock	2.51 W/m·K
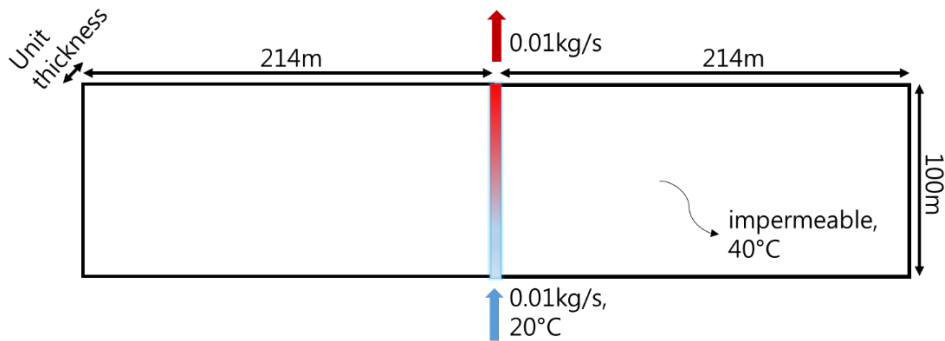
Figure 2.9: Schematic of a single fracture model used in the verification study of thermo-hydraulic responses in TOUGH2
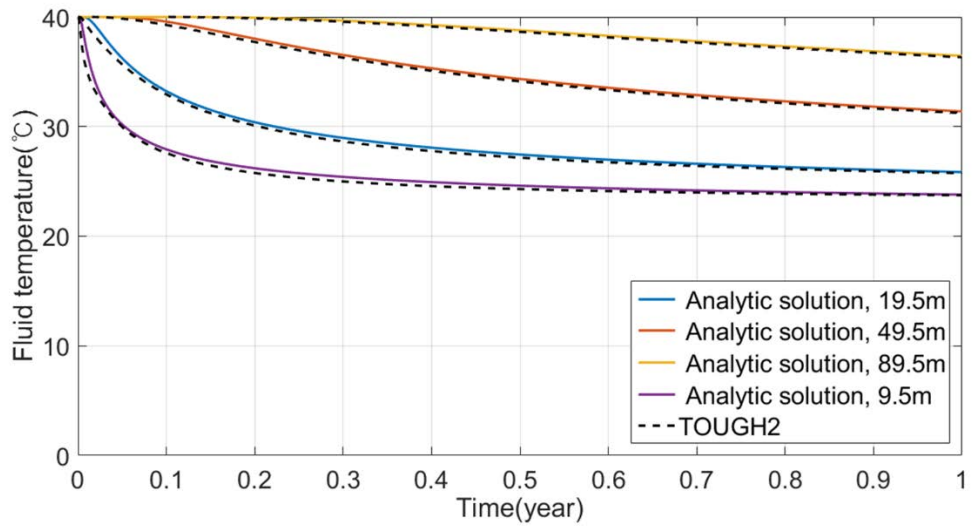
Figure 2.10: Verification of heat transfer in TOUGH2 in comparison with an analytic solution by Gringarten et al. (1975).

Chapter 3. **Hydraulic stimulation model**

A three dimensional model is built consisting of a fracture zone, rock matrix zone, and well elements (Figure 3.1). In this model, the dip direction of the fracture zone is set to be 25°, and x−direction is 205° from the north in order to have the fracture zone perpendicular to the x−z plane. The fracture zone in the model dipped 70° and its thickness is assumed to be 3.3 m. The modeling is conducted using TOUGH−FLAC. Well elements that connect the surface to the fracture zone is implemented only in TOUGH2 and water is injected into the top well element. By adjusting the size of the well elements, the pressure gradient right after the injection starts is calibrated.
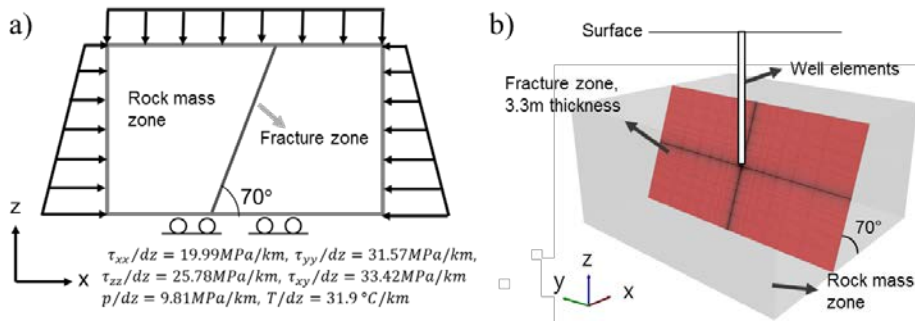
Figure 3.1: Model configuration. (a) Boundary and initial stress, pore pressure and temperature conditions, (b) Model geometry including a fracture zone in red and a rock matrix zone in gray

Table 3.1: Properties used both in PX-1 and PX-2 simulation

Properties	Value
Elastic modulus (E)	33.49 GPa
Poisson's ratio (**ν**)	0.21
Rock density	2628 kg/m^3
Porosity of rock mass	0.0048
Permeability of rock mass	$6.74\times10^{-17}\,m^2$

The in-situ stress condition of the baseline scenario is 130° of maximum horizontal stress azimuth and 1.7 of maximum and minimum horizontal stress ratio (Park et al. 2018b). The selection of the in-situ stress condition was based on studies in the Pohang EXP-1 well (Kim et al. 2017a) and the CO_2 geological storage pilot site (Chang et al. 2016). The gradients of normal and shear stress components are calculated based on the in-situ stress condition given as Figure 3.1a. The hydrostatic pore pressure is applied and temperature gradient is calculated under the assumption that 6 ℃ of surface temperature and 140 ℃ of temperature at 4.2 km deep. Fixed pore pressure and stress boundary condition is applied on the top and lateral boundaries and a roller boundary is applied on the bottom. In this study, rock temperature is assumed to be constant and thermal stress is not considered. The temperature is still taken into account in order to determine water properties in TOUGH2. The rock mass

zone has constant hydraulic and mechanical properties obtained from lab tests of rock cores from PX－2 (Kwon et al. 2018) shown as Table 3.1.

3.1 PX-1 model

In PX−1 simulation, hydroshearing and jacking on the fracture zone is simulated simultaneously. The PX−1 stimulation model is built with a size of 3,700 m×4,000 m×2,000 m in x, y, and z direction, respectively. The size is large enough not to disturb the boundary stress and pore pressure condition during the 2−day stimulation. We assumed that the fracture zone is intersecting the openhole section at the middle of the openhole section, at the depth of 4,068.5 m and this is the center of the model. A pore pressure increase of 14.8 MPa is obtained as the critical pore pressure for shear at this depth using a hydroshearing estimation program (Park et al. 2018a), which is based on an analytic model under the Mohr−Coulomb failure criterion.
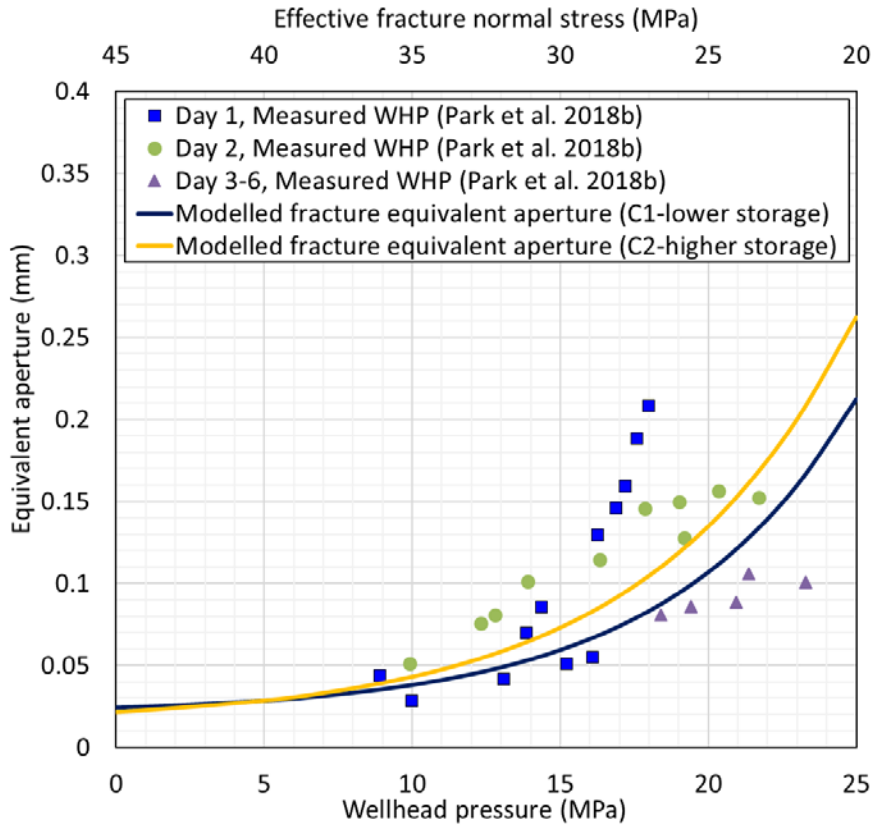
Figure 3.2: Equivalent aperture versus wellhead pressure from the field observation (dotted plot) and the elastic component of equivalent aperture against effective fracture normal stress used in the simulation (solid lines) (modified from Park et al. (2018b)).

Table 3.2: Properties applied in PX-1 simulation

Properties		Values	
Porosity of fracture zone		0.048	
Initial joint friction angle		26.6˚	
Residual joint friction angle		22˚	
Dilation angle		10˚	
Critical plastic shear strain		0.0001	
		Case 1	Case 2
Pore compressibility (Cpp)		3.6083×10^{-10} (/Pa)	1.0825×10^{-8} (/Pa)
Elastic hydraulic aperture of fracture zone ($\boldsymbol{b_{elastic}}$)	b_r	2.1×10^{-5} m	1.5×10^{-5} m
	b_{max}	0.0047 m	0.0045 m
	d	1.60×10^{-7} m	1.45×10^{-7} m

After sensitivity analysis, the critical plastic shear strain of 0.0001 and the residual friction angle of 22° is used in this study. Initial joint friction angle of 26.6° is obtained from lab test (Kwon et al. 2018). The shear dilation angle of the fracture zone is assumed to be 10° and the maximum shear dilation of 60 µm is applied, where the thickness of fracture zone is 3.3 m and the critical shear strain is 0.0001. The maximum shear dilation is also selected after a sensitivity study in order not to have a too large pressure drop during the 2-day injection period and in order to observe meaningful pressure decreases induced by shear dilation.

For the calibration of elastic equivalent aperture, the relationship between the equivalent aperture and wellhead pressure obtained from field observation is first considered. As given in Figure 3.2, the equivalent aperture increases with wellhead pressure steeply on the first day of injection. On the Day 2 and Day 3−6, the gradient of equivalent aperture over wellhead pressure became more stabilized. This may be because on the first day, the equivalent aperture calculated based on the wellhead pressure represents the hydraulic aperture of smaller area; in contrast, the calculated aperture on the following days represents that of larger area as the pressure front reaches further. Thus, we considered that the hydraulic aperture relationship of an element would be the most similar to that calculated from the first day's field observation. Secondly, it is considered that once shearing happens in a fracture element, the elastic hydraulic aperture in the element will be smaller than the actual hydraulic aperture, which is the sum of the elastic hydraulic aperture and shear dilation. Therefore, the elastic hydraulic aperture of the fracture zone is selected to be smaller than the calculated hydraulic aperture on the first day from the field on the consideration of the shear dilation. Two cases of elastic hydraulic aperture were finally chosen after the calibration process (Figure 3.2 and Table 3.2).

The fracture specific storage is the product of the fracture porosity and compressibility, and they are uncertain factors that cannot be decided from the lab test with ease. Higher specific storage

leads to a slow pressure increase and low spatial pressure development. When fracture porosity is set to be 0.0048 in the simulation, as same as rock porosity, the simulated pressure curve is significantly deviated from the measured pressure curve in the field. Small cracks can improve the specific storage although they do not play a role in permeability (Wassing et al. 2014) and the mechanical aperture of fractures is higher than hydraulic aperture (Olsson and Barton 2001). Considering these points, ten times higher porosity, 0.048, is used for the fracture zone porosity in this study. In the simulation of PX-1 stimulation, we simulate two cases, which are different to each other in fracture specific storage. Case 1 has lower specific storage, that is, lower pore compressibility than Case 2. Case 1 and 2 have slightly different elastic hydraulic aperture functions for better agreement of pressure curve in each case.

3.2 PX-2 model

A 1,450 m×1,420 m×1,520 m model is generated for hydraulic stimulation in PX-2. The size of PX-2 model is decided to be large enough to test the 2-day injection. The openhole section is 140 m at 4,208 m ~ 4,348 m deep and the center of the model is set to be in the middle of the openhole section, 4,278 m deep. The well elements intersect the fracture zone through the 140 m in z direction. The low injectivity in PX-2 was estimated to be due to wellbore damage, blocking the flow path on the pre-existing fracture (Park et al. 2018b). In the model, there is a damage zone that covers fracture elements along the openhole section. Because the extent and the area of the damage is uncertain, the property and size of the damage zone has to be assumed. The damage zone is assumed to have a hundred times lower permeability than rock permeability. The damage zone is one-meter thick and layered to 8 m, and 180 m in vertical direction covering the 140-meter openhole section (Figure 3.3).
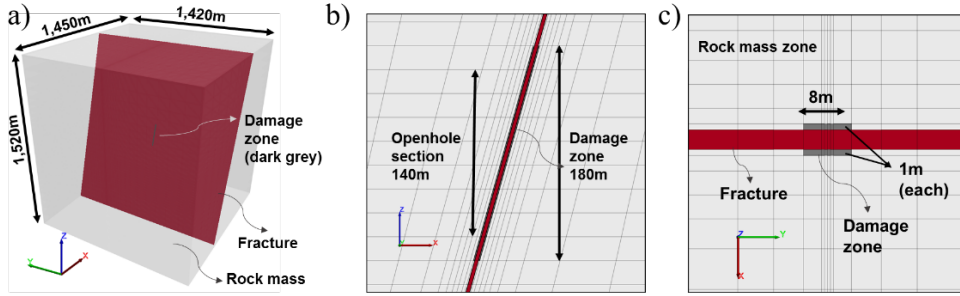
Figure 3.3: Geometry of PX-2 model. (a) Entire image of the model (b) Section view crossing the injection elements (c) Plan view intersecting an injection element.

Instead of modeling hydraulic fracturing in PX−2, we have decided to model only jacking behavior on the preexisting fracture zone as a strong jacking phenomenon was indicated in the field data without modeling hydraulic fracturing itself. As shearing and fracturing is not considered, the fracture zone is under elastic model in FLAC3D as well as the damage and rockmass zone. To describe low permeability in the damaged fracture, the permeability of the fracture zone at low wellhead pressure is set to be lower than the rock permeability. The calibrated hydraulic aperture follows the trend of the measured wellhead pressure (Figure 3.4 and Table 3.3). The reason why the calibrated equivalent aperture is lower than the measured wellhead pressure would be that the rockmass also plays a role in water flow due to the low fracture permeability at low pressure.
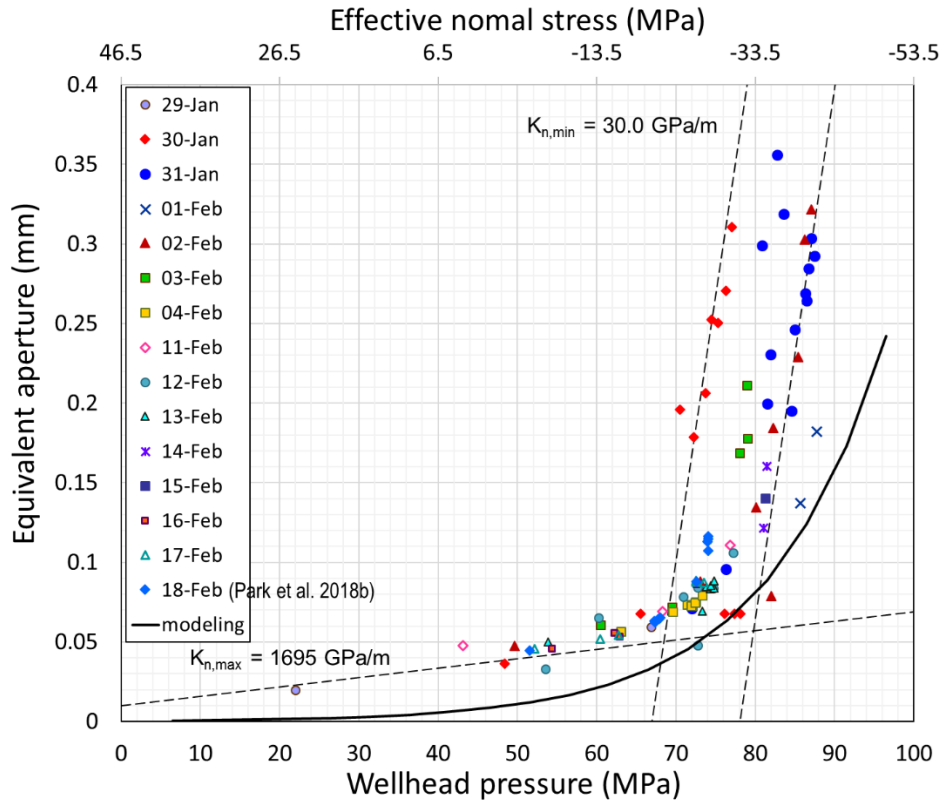
Figure 3.4: Measured equivalent aperture versus wellhead pressure and modelled equivalent aperture versus effective fracture normal stress (modified from Park et al. (2018b))

Table 3.3 Hydraulic properties applied in PX-2 simulation

Zone	Permeability	Elastic hydraulic aperture		
		b_r	b_{max}	d
Fracture zone	–	0 m	8.5×10^{-6} m	6.70×10^{-8} m
Damage zone	$6.74\times10^{-19}\,\mathrm{m}^2$			–

42

Chapter 4. **Results of stimulation model**

4.1 PX-1 model

The simulation reproduced the wellhead pressure versus time curves obtained from the 2－day injection on Dec 15－16, 2016. The calibration for the reproduction was conducted with the two main objectives: reproduction of shear induced pressure drops especially observed on the first day and general agreement with field pressure curve to explain the hydro－mechanical behaviors. Figure 4.1a shows the simulated pressure of Case 1 and Case 2 and the measured wellhead pressure on the first day of injection. The first day can be divided into three stage; about 1.1 L/s of continuous injection and shut－in in the first stage, about 1.8 L/s of injection and shut－in in the second stage, and a step rate test reaching up to 10.4 L/s of injection rate in the third stage.
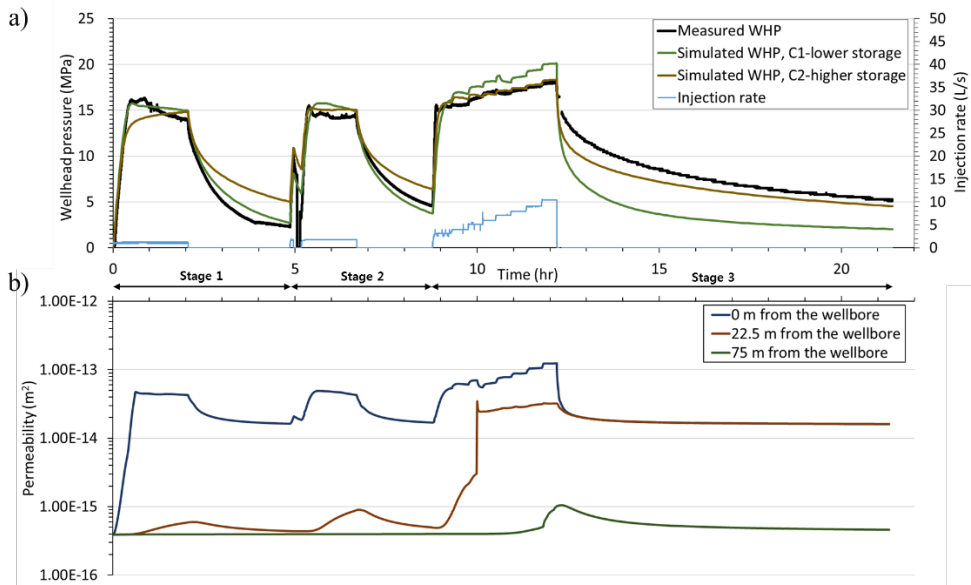
Figure 4.1: Simulation result on the first day for 21-hour hydraulic stimulation in PX-1. (a) Measured wellhead pressure from the field and simulated wellhead pressure in Case 1 and Case 2 and injection rate (b) Permeability at 0 m, 22.5 m, and 75 m from the injection well in horizontal direction on the fracture in Case 1

The simulation of Case 1 resulted in a general agreement of wellhead pressure in the first and second stage. Especially, in the first stage, a wellhead pressure peak at 15.8 MPa appeared. The peak pressure was followed by a shear that started at the critical pore pressure at the injection fracture element and it continuously decreased with a gradual increase of shear area until shut−in. Although the value of simulated pressure did not exactly match with the measured wellhead pressure, we observed a good agreement quantitatively in Stage 1 and 2 in Case 1. In the third stage, a small increase of pressure from 15 to 18 MPa during injection was measured compared to the increasing injection rate in the field. This

44

was because of the combination of continuous increase of sheared area and jacking. However, the simulated curve in Case 1 could not quantitatively match the measured increasing pressure during the injection and decreasing pressure from 18 to 5 MPa after shut−in in the third stage. In particular, the simulated pressure after shut−in in Stage 3 dropped greater than the measured pressure.

An increased specific storage was applied in Case 2. Case 2 showed relatively better agreement in the third stage than Case 1 but there was discrepancy in the first and second stages. The reason why Case 2 had a better match in Stage 3 than Case 2 is that the increased specific storage led to a slower pressure increase and decrease. This feature made good agreement of Case 2 in Stage 3, but in contrast, bad agreement in Stage 1 and 2.

Figure 4.1b presents permeability at fracture elements located at 0 m, 22.5 m, and 75 m from the injection fracture element in the horizontal direction in Case 1. At 0 m from the wellbore, that is, at injection fracture element, the permeability increased in the order of hundreds times as shearing happens with the drastic pressure increase at the first stage. Then, permeability changed proportional to the wellhead pressure change at the element. This is because the exponential function of effective normal stress was applied for the equivalent aperture. This describes jacking on the fracture zone. At 22.5 m from the borehole, permeability did not increase significantly for the first stage, as pressure front did not reach the element. In the

45

second stage, the permeability at 22.5 m increased drastically with shearing. The hydraulic stimulation in Case 1 simulation had a negligible influence on the fracture element 75m from the well for the first day. In the two cases, the residual permeability increased from $15-21$ μm to $75-81$ μm with $57-125$ times of a permeability increase when a fracture element was fully sheared.
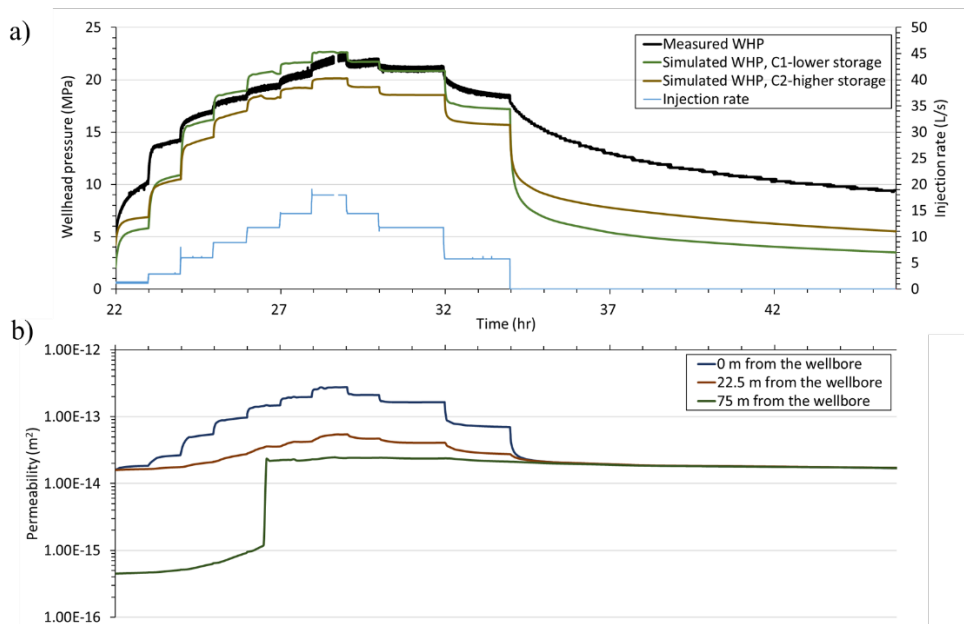

Figure 4.2: Simulation result of the 2nd day of hydraulic stimulation in PX-1 (a) Measured wellhead pressure from the field and simulated wellhead pressure in Case 1 and Case 2 and injection rate (b) Permeability at 0 m, 22.5 m, and 75 m from the injection well in horizontal direction on the fracture in Case 1

The hydraulic stimulation from the second day was simulated in Case 1 and Case 2 (Figure 4.2). On the second day, there was a step rate test increasing the injection rate from 1.1 L/s to 14.4 L/s and decreasing back to 5.8 L/s and a shut−in. The general trend of the pressure curve was generated in Case 1 and Case 2, but the simulated pressure was not matched the measured pressure in the all period. In Case 1, it started at lower pressure, reaches higher pressure at the peak injection rate and reduced to lower pressure with decreasing injection rate than the measured pressure. A problem of Case 1 was that increased pressure while injection did not maintain, and it droped drastically right after a decrease in injection rate or shut−in. In Case 2, specific storage was smaller so the pressure changes were also smaller. Thus, the agreement while reducing injection rate improved in that pressure was kept higher than Case 1, but the maximum pressure did not reached the measured maximum pressure.

The permeability of fracture elements at 0 m and 22.5 m from the injection element changed only by jacking on the as they were fully dilated by shear on the first day in Case 1. The fracture element permeability ranged from $1.6\times10^{-14}\,\mathrm{m}^2$ to $2.8\times10^{-13}\,\mathrm{m}^2$ at 0 m and $1.6\times10^{-14}\,\mathrm{m}^2$ to $5.4\times10^{-14}\,\mathrm{m}^2$ at 22.5 m from the injection. The permeability range was wider at 0 m than 22.5 m because the pore pressure change was largest at the injection element. At the fracture element 75 m from the injection, permeability gradually increased at first due to increasing pore pressure, and rapidly increased at 26−

27 hours by shearing. Because pressure did not increase enough to cause a fracture opening-up by jacking on the element at 75 m, the permeability of the element was relatively constant after shear. (Figure 4.2b).
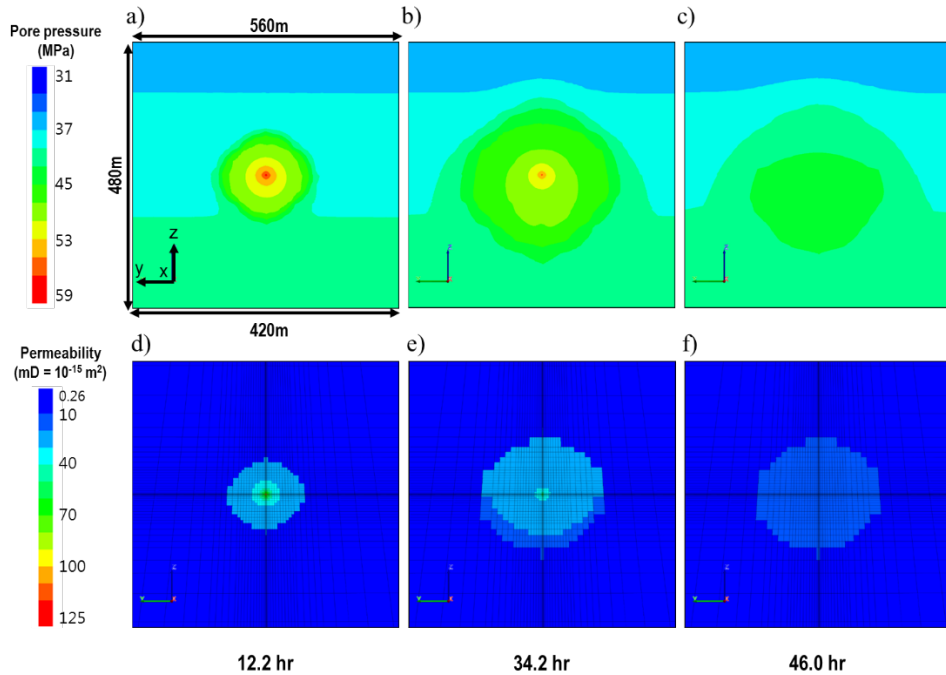
Figure 4.3: Distribution of pore pressure (a-c) and permeability (d-f) on the fracture zone at 12.2 (Day 1), 34.2 and 46.0 (Day 2) hours from the start of the stimulation of PX-1 in Case 1.

As shown in Figure 4.3a−c, pore pressure was radially developed on the fracture from the injection element. In Case 1 as a base case, the pressure disturbance front reached about 90 m and 200 m at the last shut−in of Day 1 (12.2 hours) and Day 2 (34.2 hours), respectively. Permeability improvements were apparent up to 70 and 110 m from the injection element in each of Figure 4.3d and e. Because an increase in permeability by shear occured when the pore pressure met the critical pressure for shear, the area of increased permeability was smaller than the pressure disturbance. As the equivalent hydraulic aperture was exponential function of effective normal stress on the fracture, permeability was higher near the injection element during injection. At 46 hours after the stimulation start, permeability remained increased although pore pressure dispersed after shut−in. This is due to permanent permeability increases by shear dilation. Another aspect to point out is that a slight upward increase in permeability was observed since effective normal stress lowered upwards. This is because the stress gradient was higher than pore pressure gradient in z direction due to higher density of rock mass than water.
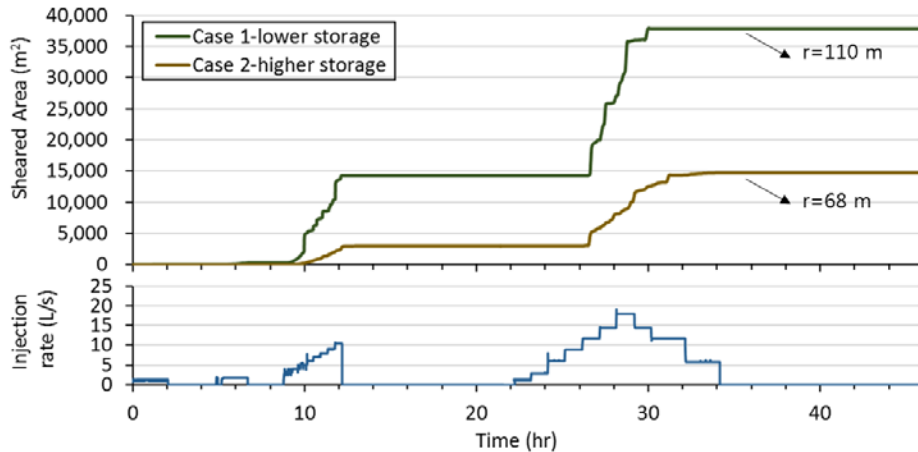
Figure 4.4: Sheared area on the fracture versus time for 2 days in Case 1 and 2 of the simulation of PX-1 hydraulic stimulation.

The shear displacement was maximum in y direction, which confirms previous studies (Chang et al. 2016; Kim et al. 2017a) that the in-situ stress state in Pohang is in a strike-slip fault regime. As shown in Figure 4.4, shearing occurred up to radius of 110 m and 68 m in Case 1 and Case 2, respectively when sheared area was assumed to be circles. Shearing was in larger area in Case 1 than in Case 2, and this was because Case 1 had a lower pore compressibility in fracture. Shear area notably increased after some hours of injection as water was accumulated for example at 10 and 26 hours from the start of the stimulation. In contrast, the increase in sheared area was negligible after shut-in in the simulation; thus, the simulation could not model shears in new area during shut-in period. However, micro seismic events had been observed during shut-in periods as well as injection periods in the hydraulic stimulation, and

the largest event had been in a shut-in period (Park et al. 2018b).

4.2 PX-2 model

The simulation of hydraulic stimulation in PX−2 reproduced the wellhead pressure versus time curves on the first two days of the stimulation, Jan 29−30, 2016. On the first day of the hydraulic stimulation, injections at the injection rate of 4−8 L/s and shut−ins were repeated 11 times for less than 10 minutes each, and an injection for 48 minutes and a shut−in was followed. The simulation of the first day firstly aimed to reproduce the repetitive increases and decreases in wellhead pressure corresponding to the injections and shut−ins. The second feature to reproduce was the stabilized wellhead pressure at around 67 MPa observed at the last injection period (Figure 4.5a). During the calibration process, we have found that the rock mass permeability, 6.74×10^{-17} m^2, measured from the lab test (Kwon et al. 2018) was too high to have simulated pressure as high as the measured wellhead pressure without any damage zone. Therefore, it is highly likely that the openhole section intersected to the rockmass were damaged as well as that to the fracture zone.
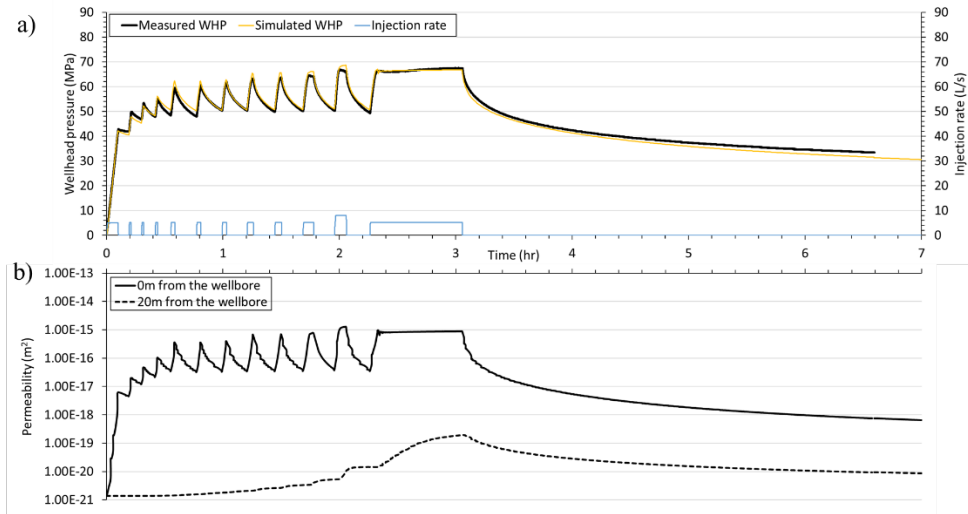
Figure 4.5: Simulation result of the 1st day of hydraulic stimulation in PX-2 (a) Measured wellhead pressure from the field, simulated wellhead pressure and injection rate (b) Permeability at 0 m and 20 m from the injection well in horizontal direction on the fracture

In Figure 4.5a, the simulated wellhead pressure on the first day is in good agreement with the measured wellhead pressure in the field with the calibrated fracture permeability (Figure 3.4 and Table 3.3). The calibration was conducted changing parameters of equivalent aperture of the fracture zone in Eq. (2.22), particularly considering the value of effective normal stress at which the equivalent aperture started to increase sharply and the equivalent aperture at tensile effective normal stress. The stabilized wellhead pressures observed around 67 MPa in the last three injection periods were reproduced as permeability increased rapidly at high pore pressure. However, there were slight discrepancies in that measured

pressure slightly dropped, but simulated pressure was increasing at the peak pressure of the second and third last injection periods. It is possible that the pressure drop was observed due to hydraulic fracturing in the reservoir. Because the simulation did not consider fracturing, it could be a reason for the discrepancy. Permeability at the injection fracture element (0 m) changed having a similar tendency to the simulated wellhead pressure. At 20 m from the wellbore in horizontal direction, permeability on the fracture element increased up to about 10^{-19} m^2, which was small compared to surrounding rock mass permeability (Figure 4.5b).
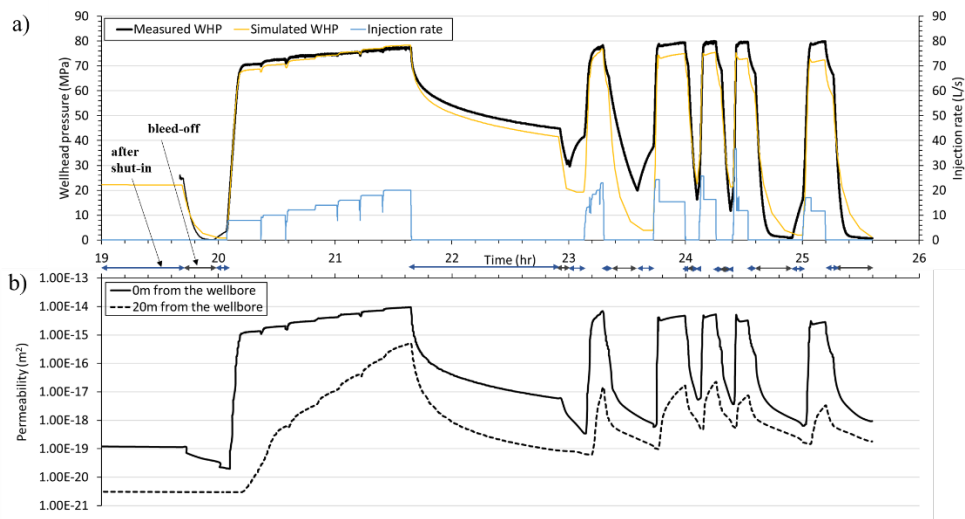

Figure 4.6: Simulation results of the 2nd day of hydraulic stimulation in PX-2. (a) Measured wellhead pressure from the field, simulated wellhead pressure, and injection rate (b) Permeability at 0 m and 20 m from the injection well in horizontal direction on the fracture

54

The simulated pressure curve on the second day also generally followed the measured wellhead pressure in the field (Figure 4.6a). There had been bleed−offs on the second day of the stimulation, but the exact amounts or rate of back−flow water had not been measured during the test. By calibration, the productivity index of $2.5{\times}10^{-13}$ m^3 was used on the well element for all the bleed−offs. The simulation could not achieve agreement with the measured wellhead pressure in all the bleed−off periods. One notable result is that the gradual increase in pressure from 20.1 to 21.6 hours was reproduced in good agreement by the simulation. However, pressure declined more than the measured pressure after shut−in at 21.6 hours and during all the following injection periods, the simulated pressure was about 5 MPa lower than the measured pressure.
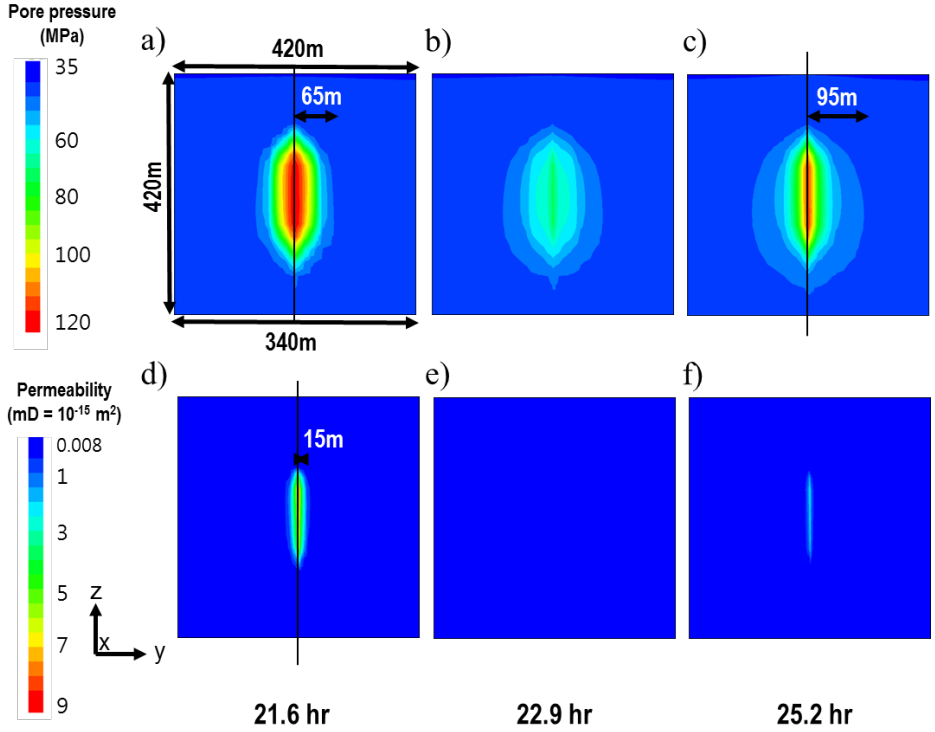
Figure 4.7: Permeability (a-c) and pore pressure (d-f) distribution on the fracture zone at 21.6, 22.9, and 25.2 hours in simulation of PX-2 hydraulic stimulation

Permeability changes depending on the pore pressure was well captured by the simulation as given in Figure 4.7. At 21.6 hour, after a 1.6-hour step rate test, the pore pressure front reached 65 m on the fracture in horizontal direction, and the permeability increased to in the order of 10^{-15} m^2 up to 15 m from the well (Figure 4.7a and d). There was a shut-in at 21.6 hours and no injection to 22.9 hours. In Figure 4.7b, the high pressure near the well was eased as the water was diffused at 22.9 hours, and consequently, permeability was dropped closing the permeable flow path in Figure 4.7e. Compared to the pore pressure distribution, permeability increases to 10^{-15} m^2

56

appeared in a narrow area. This is because around 70 MPa of additional pore pressure to the hydrostatic pressure was required to observe the 10^{-15} m^2 of the permeability, and that much highly pressurized area was far smaller than the total pressure disturbance area. The pressure front reached 95 m in horizontal direction at a maximum at the moment of the last shut–in in Day 2, but the area as permeable as 10^{-15} m^2 was slight near the well (Figure 4.7c and f).

Chapter 5. **Circulation model**

5.1 Model description

A circulation model is generated by extending PX−1 and PX−2 stimulation models. The size of model is 4,000 m, 3,900 m and 3,130 m in x, y and z direction, respectively. The model is composed of a a rock mass zone and a fracture zone inclined at 70°. The thickness of the fracture zone is applied to be 3.3 m, which is identical to those of the hydraulic stimulation models. PX−1 and PX−2 are 600 m apart in y direction in the model, following the bottomhole distance of 616 m presented in Park et al. (2018b). In this model, well elements are implemented only at the bottom holes where the well elements are intersecting with the fracture zone. Same as the PX−1 and PX−2 stimulation models, a well element of PX−1 is adjoined to the fracture zone at the depth of 4,068.5 m, in the middle of the openhole section and those of PX−2 is located at the depth of 4,208 m ~ 4,348 m along the openhole section on the fracture plane (Figure 5.1).
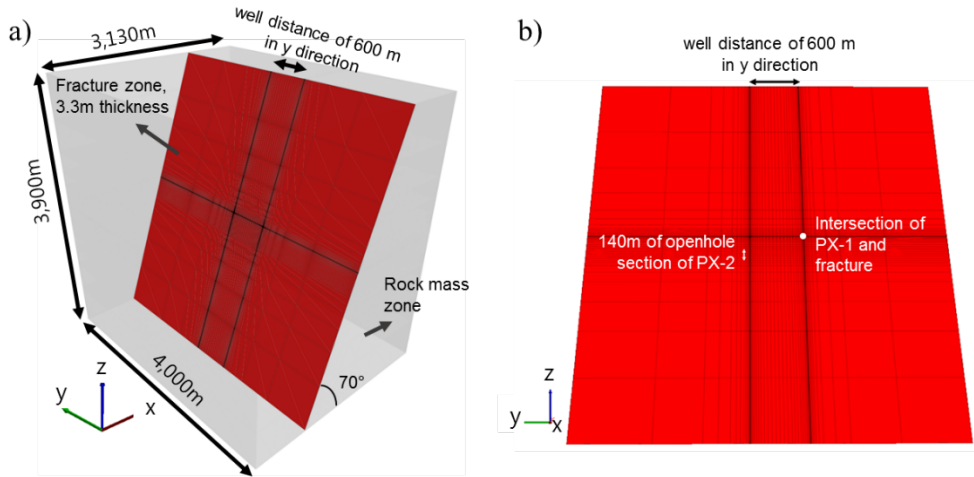
Figure 5.1: Schematic of the circulation model. (a) Geometry including a fracture zone and rock mass zone, (b) Mesh of the fracture plane and location of well elements

Table 5.1 Properties applied in the circulation model

Properties	Values
Permeability of rock mass zone	$6.74 \times 10^{-17} \, \text{m}^2$
Porosity of rock mass zone	0.0048
Porosity of fracture zone	0.048
Thermal conductivity of rock	3.0 W/m·K
Specific heat of rock	800 J/kg·K
Rock density	2628 kg/m^3

The initial pressure and temperature has a linear gradient of 9.81 MPa/km and 31.9 ℃/km, increasing the values as getting deeper. The hydrostatic pressure is applied having 0.1 MPa on the surface. Based on a measurement of 140 ℃ at 4.2 km deep and an assumption of 6 ℃ of surface temperature, the temperature is decided. Constant pressure and temperature boundary condition is applied. The initial bottomhole temperature and pressure are 135.79 ℃ and 40.01 MPa at PX-1 and 140.25 ℃ and 41.39 MPa at PX-2. Hydraulic and thermal properties are mainly obtained from a lab test results of PX-2 cores from 4.2 km depth (Kwon et al. 2018). Porosity of rock mass zone is an uncertain property, and it is assumed to be 10 times larger than the rock mass porosity, which is same as that in the stimulation models (Figure 5.1).

Three different values of fracture permeability are tested in this study. One is the calibrated residual permeability of Case 1 in the PX-1 stimulation model, 1.6×10^{-14} m^2, which was shown in Chapter 4.1. The second one is a thousand times of intact rock permeability and about 42 times of the calibrated residual permeability, 6.74×10^{-13} m^2. The last one is ten thousand times of rock mass permeability and about 420 times of the calibrated residual permeability, 6.74×10^{-12} m^2. It is assumed that the fracture plane is a fully sheared and has uniform permeability. Mechanically induced permeability changes are

not considered in this model as the stress dependent permeability changes at lower than wellhead pressure of 10 MPa are not significant as shown in Figure 3.2 and 3.4. Thus hydrothermal models, excepting mechanical behaviors, are simulated in TOUGH2.

Water at enthalpy of 2.84474×10^5 J/kg (60 ℃ at 40 MPa approximately) is injected to one well and produced from the other well at 40 kg/s of constant flow rate. Two sets of injection and production wells are tested: injection at PX－1 and production at PX－2 and injection at PX－2 and production at PX－2. Pressure at both injection and production well is measured and it is evaluated whether the reservoir is productive itself. 10 MPa is selected to be the maximum allowable pressure changes at the bottomholes following an example given in Tester et al. (2006). For temperature drawdown of production, 10 ℃ for 30 years of operation is chosen to be a target based on Beardsmore et al. (2010). To sum up, simulating the circulation at the three cases of fracture zone permeability, we estimated the pressure and production temperature at bottomhole and evaluated sustainability for 30 years.

5.2 Simulation results

In the circulation model, three cases of fracture permeability were applied to two sets of injection and production wells: production and injection at PX-1 and PX-2 and at PX-2 and PX-1, respectively. First of all, 1.6×10^{-14} m^2 was used for the fracture permeability, which was the fully-sheared residual permeability of Case 1 in the simulation of stimulation in PX-1. This was to analyze the feasibility of the reservoir assuming that the whole area of the fracture zone was possible to be fully stimulated up to the maximum shear dilation. However, the simulation at this permeability instantly stopped right after the initiation as pressure at PX-1 reached the prescribed pressure limits. In the case of injecting at PX-1 and producing at PX-2, pressure at PX-1 reached 200 MPa at 0.8 second after the onset. When water was injected at PX-2 and produced at PX-1, pressure at PX-1 decreased to 0.1 MPa after 10 seconds of injection. This result demonstrates that the fracture zone has to be stimulated by more than the maximum dilation of 60 μm in order to self-pump by itself.

Subsequently, we aimed to find to what extent the permeability of the fracture zone has to be increased to produce at 40 kg/s, and to estimate production temperature for a 30-year operation with such fracture permeability. Two cases of permeability, 6.74×10^{-13} m^2 and

$6.74 \times 10^{-12}\,\mathrm{m}^2$, were tested for that purpose.
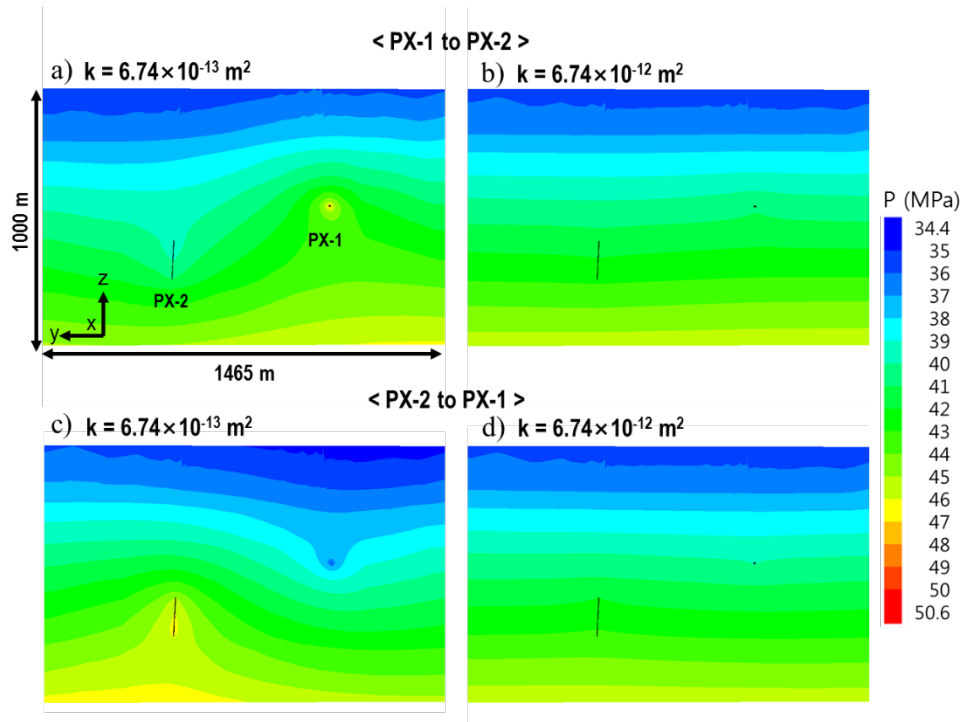
Figure 5.2: Pressure distribution on a magnified fracture plane (1,465 m×1,000 m) when fracture permeability is 6.74×10^{-13} m^2 and 6.74×10^{-12} m^2 and injection and production is from PX-1 to PX-2 and from PX-2 to PX-1 ((a) to (d) each) at 30 years of circulation. Black marks indicate the well location.

Simulated pressures were measured at PX−1 and PX−2 for 30 years of circulation in the four cases. When fracture permeability was $6.74 \times 10^{-13} \, \text{m}^2$, pressure at PX−1 changed more than 10 MPa in the both sets of injection and production wells. Injecting to PX−1 and producing from PX−2, pressure at PX−1 reached 75.6 MPa, whereas pressure at PX−2 ranged to 40.6 MPa. When injecting water in the reverse, from PX−2 to PX−1, pressure at PX−1 reduced to 20.6 MPa being stabilized, but the pressure change at PX−2 was much smaller increasing to 46.5MPa. Pressurization at the injection well and depressurization at the production well was clearly observed as shown in Figure 5.2a and c. It is shown that fracture permeability of $6.74 \times 10^{-13} \, \text{m}^2$ was not permeable enough to continue the circulation without a massive support by pump work.

With increased fracture permeability to $6.74 \times 10^{-12} \, \text{m}^2$, much higher injectivity and productivity were observed, having pressure changes less than 5 MPa at the two wells with the both sets of injection and production wells. When circulating water from PX−1 to PX−2 in the reservoir, steady pressure was 43.9 MPa and 43.1 MPa at PX−1 and PX−2, respectively. In the case of injection to PX−2 and production from PX−1, pressures converged to 43.1 MPa and 38.6 MPa at PX−2 and PX−1 respectively. In Figure 5.2b and d, pressure disturbance was not distinct compared to Figure 5.2a and c. The small amount of pressure changes enabled a continuous self−circulation of water thorough the reservoir and wells.
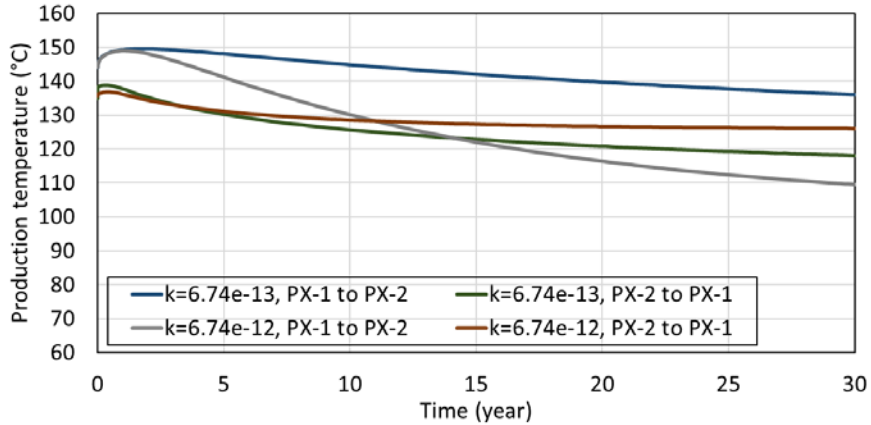
Figure 5.3: Production temperature for 30 years of operation in the four cases (two cases of fracture permeability, 6.74×10^{-13} m^2 and 6.74×10^{-12} m^2; two sets of well, circulation at downhole from PX-1 to PX-2 and from PX-2 to PX-1).

Production temperature for 30 years was measured in the four cases as shown in Figure 5.3. Temperature disturbance area developed radially and a tip of the disturbance area pointed to the production well (Figure 5.4). When fracture permeability is 6.74×10^{-13} m^2, production temperature slightly increased for 1-2 years in the beginning and then, kept decreasing for the rest of the period. Production temperature ranged from 150 ℃ to 136 ℃ producing at PX-2, and from 139 ℃ to 118 ℃ producing at PX-1. Production water was hotter at a production well of PX-2 than that of PX-2. The reason for the higher production temperature at PX-2 is highly likely to be due to the higher initial temperature at the deeper depth at PX-2.
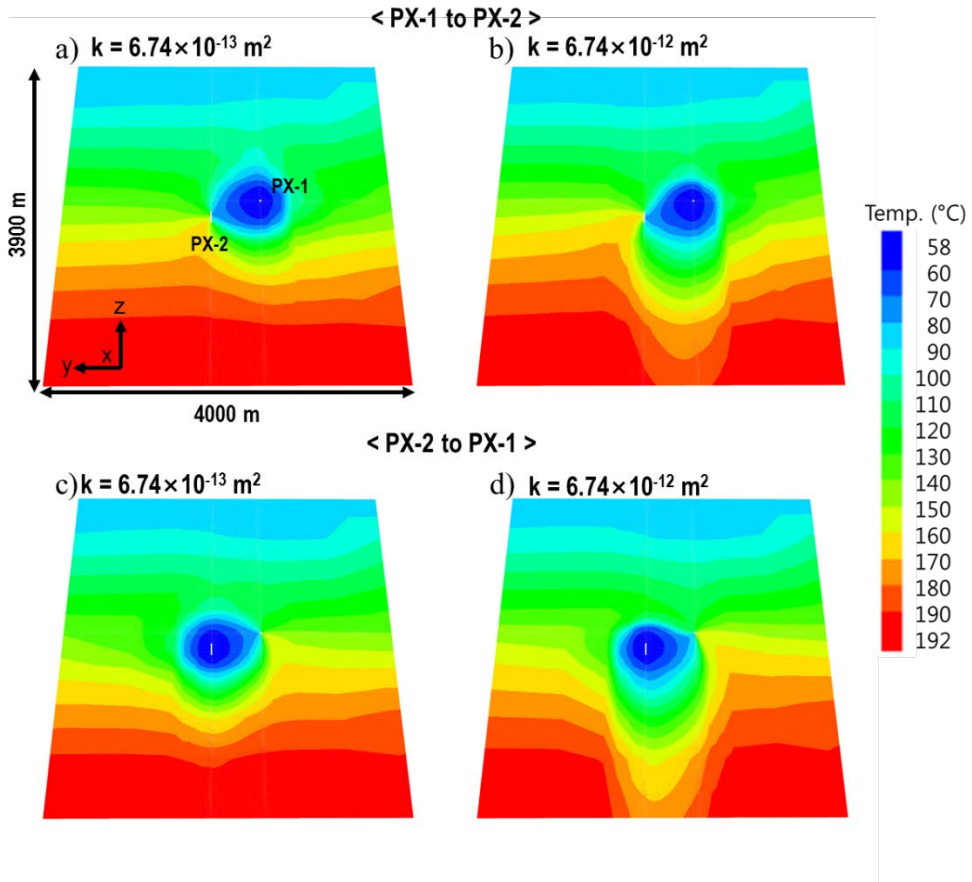
Figure 5.4: Temperature distribution on the fracture plane when fracture permeability is 6.74×10^{-13} m^2 and 6.74×10^{-12} m^2 and injection and production is from PX-1 to PX-2 and from PX-2 to PX-1 ((a) to (d) each) at 30 years of circulation. White marks indicate the well location.
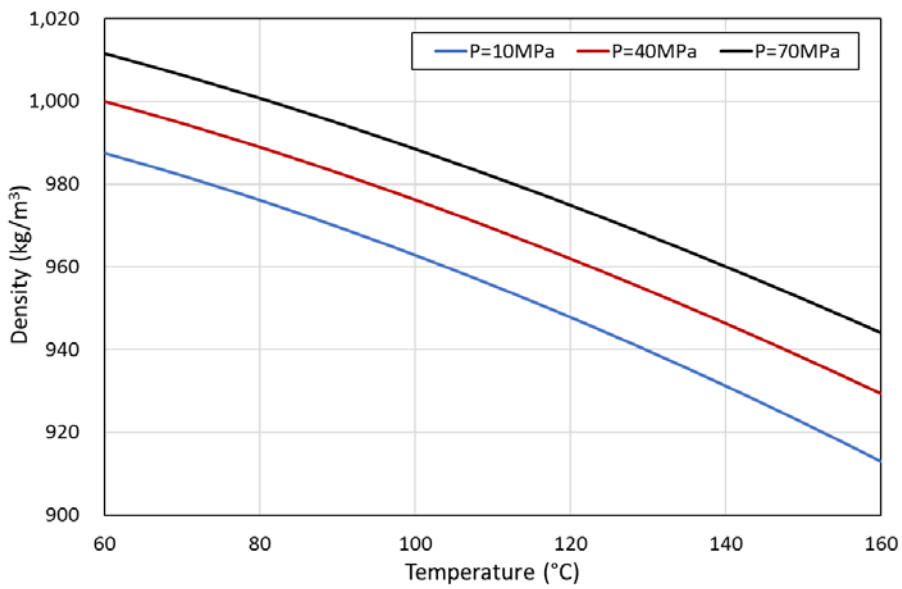
Figure 5.5: Water density with respect to temperature and pressure built in TOUGH2.
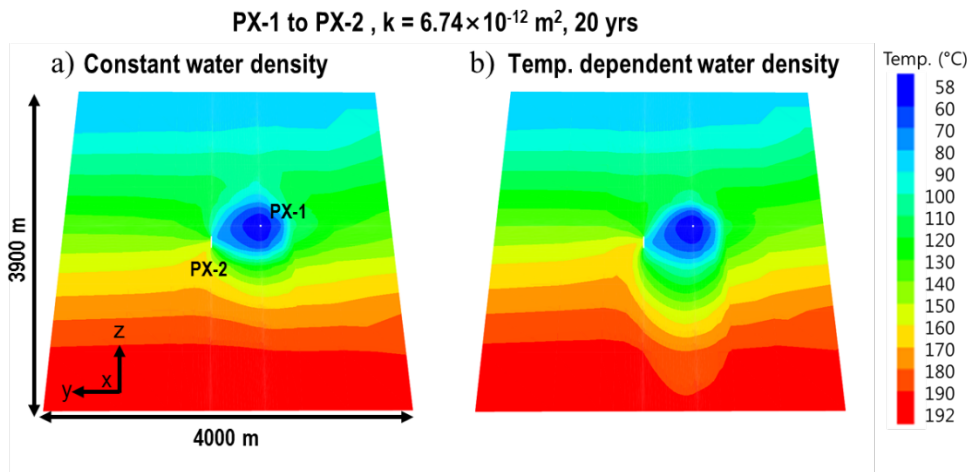
Figure 5.6: Temperature distribution on the fracture plane when fracture permeability is 6.74×10^{-12} m² and injection and production is from PX-1 to PX-2 at 20 years of circulation. (a) Constant water density, 1,000 kg/m³ (b) Temperature dependent water density built in TOUGH2. White marks indicate the well location.

67

The trend of a small increase for the first 1−2 years and a continuous decrease after the peak in production temperature also appeared when fracture permeability is $6.74 \times 10^{-12}\,\mathrm{m^2}$. The range of production temperature was 110 ℃ to 149 ℃ at PX−2 and 137 ℃ to 126 ℃ at PX−1. An interesting point is that production temperature at PX−2 decreased more with the permeability of $6.74 \times 10^{-12}\,\mathrm{m^2}$ than that of $6.74 \times 10^{-13}\,\mathrm{m^2}$. Another is that production temperature started to be cooler at PX−2 than PX−1 at 11.2 years after the circulation start.

These phenomena can be explained by the higher water density at lower temperature, and a higher water mobility on a more permeable fracture zone. First, the cold injected water moves downwards than upwards due to higher density than surrounding area. Water density decreases at higher temperature, ranging from about 1,000 to 900 kg/m^3 from 60 to 160 ℃ (Figure 5.5). Thus temperature front developed further downwards than upwards as observed in Figure 5.4. Secondly, with the higher permeability, injected cold water can move through and cools down larger area. To confirm the temperature−dependent density effect, an additional simulation with a constant water density, 1,000 kg/m^3 was conducted. In Figure 5.6, it is shown that when density is temperature dependent, the cold water moves more downwards than constant. In the comparison between Figure 5.4a and b, and between Figure 5.4c and

d, the temperature disturbance area was larger at permeability of 6.74×10^{-12} m^2 than that of 6.74×10^{-13} m^2. In the case of the lower fracture permeability, thermal drawdown occurred more intensively between and near the two wells than in the case of the higher fracture permeability.

When we produced from PX$-$2, which was deeper than PX$-$1, water moving in the direction of PX$-$1 to PX$-$2 went downwards. Injected cold water more easily reached PX$-$2 at the higher fracture permeability, 6.74×10^{-12} m^2, than the lower permeability, 6.74×10^{-13} m^2, This is because cold water dispersed larger area, and water dispersion was stronger downwards than upwards and aligned with the direction to PX$-$2. When the fracture had the higher permeability, 6.74×10^{-12} m^2, thermal drawdown at production well was higher when PX$-$2 was the production well than PX$-$1 is. Since cold water tends to move downwards and to decrease the deeper reservoir, production at the deeper well can be disadvantageous for higher production temperature in the long run. This phenomenon becomes obvious the fracture permeability is large enough like as much as 6.74×10^{-12} m^2 in this model.

The best case in terms of production temperature is the production at PX$-$2 from a 6.74×10^{-13} m^2 of fracture permeability model of which the minimum temperature is 136 ℃. The minimum thermal drawdown of production appears to be 9 ℃ when producing

at PX$-$1 in a 6.74×10^{-12} m^2 of fracture permeability model.

Chapter 6. **Discussion**

6.1 Hydraulic stimulation

Not all period of the simulated pressure in PX－1 agreed with the measured pressure. One of the possible scenarios is that the fracture zone does not follow a uniform permeability function all over the fracture plane, which makes the single fracture permeability model not able to represent the field. Considering the simulation result that the pressure did not maintain after shut－in, permeability may be lower at some distance from PX－1 than near the well. In other words, the fractures may become less permeable as getting further from the well or disconnected at some point. Another factor is the possibility of existence of small cracks that do not improve the permeability but increase specific storage in the fracture zone. The specific storage could be a time－dependently changing parameter by opening up small cracks at high pressure. Also, the assumed thickness of fracture zone, 3.3 m, may be different from the actual thickness in the reservoir. However, these fracture properties have not been measured and are difficult to measure, raising uncertainties in numerical modeling.

In PX－2, distinguishable discrepancy began to appear in the pressure curve of the second day. In particular, the simulated pressure during injection was lower than the measured pressure

after shut−in at 21.6 hours. It can be inferred that rock mass permeability may be higher than $6.74 \times 10^{-17} \, m^2$, which is the average permeability of three samples ($1.34 \times 10^{-18} \, m^2$, $3.29 \times 10^{-17} \, m^2$ and $1.68 \times 10^{-16} \, m^2$) measured in the lab test. The high deviation of permeability between the samples brings an uncertainty in the rock mass permeability. In PX−2 model, rock mass permeability is higher than the fracture permeability at pore pressure of lower than about 90 MPa (about 50 MPa of additional pore pressure), so permeability of rock mass as well as of fracture influences the pressure changes in contrast to PX−1. Therefore, the uncertainty of rock mass permeability can be one of the possibilities for the discrepancy.

In terms of the damage zone in the PX−2 model, it would be hard to determine the exact area and the extent of the damage only using this numerical model. There can be diverse combinations of area and permeability of the damage to reproduce the measured pressure curves from the field. In other words, the combination of damage properties in this study, such as the thickness of 1 m, width of 8m, the length of 180 m, and the permeability of $6.74 \times 10^{-19} \, m^2$, can suggest a probable condition of PX−2, but there is a limitation to being quantitatively defined. However, it is meaningful that the PX−2 model confirmed the high possibility for existence of damage zone by showing a good agreement with measured pressure.

6.2 Circulation model

The simulation of circulation indicates that the fracture residual permeability of 1.6×10^{-14} m^2 is not large enough to produce geothermal water at 40 kg/s at commercial interests. In other words, with the maximum shear dilation of 60 μm, the reservoir may not be able to achieve the target flow rate in the present condition although it is assumed that the whole the fracture area influential on fluid flow is to be fully sheared.

One of the possible ways to improve the injectivity would be to make full use of the long openhole section of 313 m of PX-1. An assumption in this model is the whole openhole section of PX-2 is contacting with the fracture zone since hydraulic fracturing is estimated to have occurred and the fracture by the fracturing is somehow connected to the preexisting fracture. In contrast, the openhole section of PX-1 is intersecting the pre-existing fracture zone having a contact length of 3.3 m, equal to the assumed fracture thickness. Therefore, PX-1 in this model is pressurized or depressurized more than PX-2 when injecting to or producing from the well at the same fracture permeability and flow rate.

A notable observation in the estimation of production temperature is that whether the production well is deeper or swallower than the injection well affects the production temperature.

If the well conditions are the same and permeability is suitably high for the circulation like $6.74 \times 10^{-13}\,\mathrm{m}^2$ in this model, it is favorable to produce from the deeper well where the initial and ambient temperature is higher. On the other hand, if the permeability is very high, such as $6.74 \times 10^{-12}\,\mathrm{m}^2$ in this model, drilling from the deeper borehole may be disadvantageous. However, this phenomenon would be difficult to happen in actual EGS reservoirs because increasing permeability to such a value is challenging. This could appear in a hydrothermal reservoirs combining re-injection, which has relatively higher permeability compared to general EGS reservoirs.

Chapter 7. **Conclusion**

Numerical simulation of the first hydraulic stimulation of Pohang EGS site and for a preliminary study on production estimation was conducted. First, the pressure curves from the hydraulic stimulation in the field is reproduced for the first two days of wellhead pressure data at PX－1 and PX－2 wells. Two wells with low and high injectivity each were modelled together in this study; injectivity of PX－1 and PX－2 is high and low, respectively. A single fracture zone was implemented representing the pre－existing fractures that intersect the openhole sections of the both wells. Hydro－mechanical behaviors considered in the modeling were hydraulic shearing and jacking on the pre－existing fractures in PX－1 and jacking on a fracture zone in PX－2. In particular, a pressure drawdown induced by shearing in Stage 1 of the first day was captured in the numerical simulation in PX－1. In PX－2, a jacking model could reproduce the stabilized pore pressure at wellhead pressure of 67 MPa on the first day.

In PX－1, permanent permeability enhancement by shearing is estimated to have happened to 68－110 m until the second day. The calibration resulted in changes in residual fracture permeability from 15－21 μm to 75－81 μm in maximum. In Case 1, residual fracture permeability of an element improved to $1.6 \times 10^{-14}\,\mathrm{m}^2$ by shearing and permeability reached $2.8 \times 10^{-13}\,\mathrm{m}^2$ combined with jacking. However,

simulated pressure curves were not in agreement with measured pressure in the all periods. The pressure in Case 1 successfully matched in the first and second stages on Day 1, but did not agree in the following stages since as it increases higher during injection and decreases more during shut−in. With larger specific storage, Case 2 simulated the third stage on Day 1, but simulated pressure did not increased as much as the measured pressure on the second day 2.

In the PX−2 simulation, a permeability increase to in the order of $10^{-15}\,\mathrm{m}^2$ appeared at most to 15 m from the well on the second day, but, on the other hand, pressure disturbance front reached 95 m at a maximum. This was because a significant increase in permeability occurred at additional pore pressure larger than 67 MPa. The good agreement of simulated and measured pressure confirms the jacking model in a single fracture zone. Although hydraulic fracturing was not discretely modelled, pressure curves could be reproduced using an exponential function of effective normal stress for hydraulic fracture aperture. In a future study, hydraulic fracturing can be modelled as well, and corresponding changes in stress condition can be additionally taken into account.

In conclusion, this study confirms the stimulation mechanisms estimated in the observational study in Park et al. (2018b), shearing and jacking in PX−1 and jacking in PX−2. This study also has a significance in that it is the first numerical modeling of hydraulic stimulation at PX−1 and PX−2 wells in Pohang EGS site. However,

due to a lack in seismicity location data, simulation results could not be compared with them. In addition, seismic event by shear during shut−in period in PX−1 did not reproduced in the simulation. Calibration with micro seismicity will thus improve the simulation results. Also, thermal stress and thermally induced stimulation can be considered by setting a non−isothermal condition in the further study.

The circulation model revealed that the maximum shear dilation of 60 µm, calibrated in the PX−1 stimulation model, is not large enough to circulate water at flow rate of 40 kg/s. The fracture permeability has be increased to higher than 6.74×10^{-13} m^2. Improving connectivity between the openhole sections and fracture zone should to be accompanied for a favorable operation without an excessive demand on pumps. The highest production temperature was when producing at PX−2 with fracture permeability of 6.74×10^{-13} m^2, but it requests hard pump work. Thermal drawdown was minimum at a production well of PX−1 in in a 6.74×10^{-12} m^2 of fracture permeability model. This study is a preliminary study, so this circulation model can be improved in the future with a more comprehensive study on fracture characterization.

Reference

Armstead HCH, Tester JW (1986) Heat mining

Bödvarsson GS, Tsang CF (1982) Injection and thermal breakthrough in fractured geothermal reservoirs Journal of Geophysical Research: Solid Earth 87:1031−1048

Beardsmore GR, Rybach L, Blackwell D, Baron C (2010) A protocol for estimating and mapping global EGS potential GRC Transactions 34:301−312

Blöcher MG, Zimmermann G, Moeck I, Brandt W, Hassanzadegan A, Magri F (2010) 3D numerical modeling of hydrothermal processes during the lifetime of a deep geothermal reservoir Geofluids 10:406−421 doi:10.1111/j.1468−8123.2010.00284.x

Bodvarsson G (1969) On the temperature of water flowing through fractures Journal of Geophysical Research 74:1987−1992 doi:10.1029/JB074i008p01987

Cappa F, Rutqvist J (2011) Impact of CO2 geological sequestration on the nucleation of earthquakes Geophysical Research Letters 38:n/a−n/a doi:10.1029/2011gl048487

Chang C, Jo Y, Quach N, Shinn Y, Song I, Kwon Y Geomechanical characterization for the CO 2 injection test site, offshore Pohang Basin, SE Korea. In: 50th US Rock Mechanics/Geomechanics Symposium, 2016. American Rock Mechanics Association,

Dempsey D, Kelkar S, Davatzes N, Hickman S, Moos D (2015) Numerical modeling of injection, stress and permeability enhancement during shear stimulation at the Desert Peak Enhanced Geothermal System International Journal of Rock Mechanics and Mining Sciences 78:190−206 doi:10.1016/j.ijrmms.2015.06.003

Elsworth D (1989) Theory of thermal recovery from a spherically stimulated hot dry rock reservoir Journal of Geophysical Research 94:1927 doi:10.1029/JB094iB02p01927

Genter A, Evans K, Cuenot N, Fritsch D, Sanjuan B (2010) Contribution of the exploration of deep crystalline fractured reservoir of Soultz to the knowledge of enhanced geothermal systems (EGS) Comptes Rendus Geoscience 342:502−516 doi:10.1016/j.crte.2010.01.006

Gringarten AC, Witherspoon PA, Ohnishi Y (1975) Theory of heat extraction from fractured hot dry rock Journal of Geophysical Research 80:1120−1124 doi:10.1029/JB080i008p01120

Hsiung SM, Chowdhury AH, Nataraja MS (2005) Numerical simulation of thermal−mechanical processes observed at the Drift−Scale Heater Test at Yucca Mountain, Nevada, USA International Journal of Rock Mechanics and Mining Sciences 42:652−666 doi:10.1016/j.ijrmms.2005.03.006

Itasca (2009) FLAC3D, Fast Lagrangian Analysis of Continua in 3 Dimensions, Version 4.0 Minneapolis, Minnesota, Itasca Consulting Group

Jeanne P, Rutqvist J, Rinaldi AP, Dobson PF, Walters M, Hartline C, Garcia J (2015) Seismic and aseismic deformations and impact on reservoir permeability: The case of EGS stimulation at The Geysers, California, USA Journal of Geophysical Research: Solid Earth 120:7863−7882 doi:10.1002/2015jb012142

Kim H, Xie L, Min K−B, Bae S, Stephansson O (2017a) Integrated In Situ Stress Estimation by Hydraulic Fracturing, Borehole Observations and Numerical Analysis at the EXP−1 Borehole in Pohang, Korea Rock Mechanics and Rock Engineering doi:10.1007/s00603−017−1284−1

Kim K−I et al. (2017b) Protocol for induced microseismicity in the first enhanced geothermal systems project in Pohang, Korea Renewable & Sustainable Energy Reviews (under review)

79

Kolditz O, Clauser C (1998) Numerical simulation of flow and heat transfer in fractured crystalline rocks: application to the hot dry rock site in Rosemanowes (UK) Geothermics 27:1−23

Kwon S, Xie L, Park S, Kim K−I, Kim H, Min K−B (2018) Characterization of 4.2 km deep fractured granodiorite cores in Pohang geothermal reservoir, Korea Rock Mechanics and Rock Engineering (under review)

Lee J (2014) Implicit and Explicit Fracture Shear Slip Analysis for Geological Storage of Carbon Dioxide and Nuclear Waste. Seoul National University

Lee TJ, Song Y, Park D−W, Jeon J, Yoon WS Three Dimensional Geological Model of Pohang EGS Pilot Site, Korea. In: Proceedings, 2015.

Min K−B, Rutqvist J, Tsang C−F, Jing L (2004) Stress−dependent permeability of fractured rock masses: a numerical study International Journal of Rock Mechanics and Mining Sciences 41:1191−1210 doi:10.1016/j.ijrmms.2004.05.005

Olsson R, Barton N (2001) An improved model for hydromechanical coupling during shearing of rock joints International Journal of Rock Mechanics and Mining Sciences 38:317−329

Park S, Kim K−I, Kwon S, Yoo H, Xie L, Min K−B, Kim KY (2018a) Development of a Hydraulic Stimulation Simulator Toolbox for Enhanced Geothermal System Design Renewable Energy 118:879−895 doi:10.1016/j.renene.2017.11.016

Park S et al. (2018b) Hydraulic Stimulations in Fractured Geothermal Reservoir in Pohang, South Korea − Field Observations and Analyses Rock Mechanics and Rock Engineering (in preparation)

Park S et al. (2017) First Hydraulic Stimulation in Fractured Geothermal Reservoir in Pohang PX−2 Well Procedia Engineering 191:829−837

Pruess K (1990) Modeling of geothermal reservoirs: fundamental processes, computer simulation and field applications Geothermics 19:3-15

Pruess K, Oldenburg C, Moridis G (2011) TOUGH2 User's Guide, Version 2.1, LBNL-43134 (revised) Lawrence Berkeley National Laboratory, Berkeley, CA

Rinaldi AP, Rutqvist J (2018) Joint opening or aseismic hydroshearing? Analyzing a fracture zone stimulation at Fenton Hill Geothermics (under review)

Rutqvist J (2011) Status of the TOUGH-FLAC simulator and recent applications related to coupled fluid flow and crustal deformations Computers & Geosciences 37:739-750 doi:10.1016/j.cageo.2010.08.006

Rutqvist J, Rinaldi AP, Cappa F, Moridis GJ (2015) Modeling of fault activation and seismicity by injection directly into a fault zone associated with hydraulic fracturing of shale-gas reservoirs Journal of Petroleum Science and Engineering 127:377-386 doi:10.1016/j.petrol.2015.01.019

Rutqvist J, Tsang C-F (2003) Analysis of thermal-hydrologic-mechanical behavior near an emplacement drift at Yucca Mountain Journal of Contaminant Hydrology 62-63:637-652 doi:10.1016/s0169-7722(02)00184-5

Sanyal SK, Butler SJ, Swenson D, Hardeman B (2000) Review of the state-of-the-art of numerical simulation of enhanced geothermal systems TRANSACTIONS-GEOTHERMAL RESOURCES COUNCIL:181-186

Shaik AR, Rahman SS, Tran NH, Tran T (2011) Numerical simulation of fluid-rock coupling heat transfer in naturally fractured geothermal system Applied thermal engineering 31:1600-1606

Tenzer H, Park C-H, Kolditz O, McDermott CI (2010) Application of the geomechanical facies approach and comparison of exploration and evaluation methods used at Soultz-sous-Forêts (France) and Spa Urach

(Germany) geothermal sites Environmental Earth Sciences 61:853-880 doi:10.1007/s12665-009-0403-z

Tester JW et al. (2006) The future of geothermal energy: Impact of enhanced geothermal systems (EGS) on the United States in the 21st century Massachusetts Institute of Technology 209

Vilarrasa V, Rinaldi AP, Rutqvist J (2017) Long-term thermal effects on injectivity evolution during CO 2 storage International Journal of Greenhouse Gas Control 64:314-322 doi:10.1016/j.ijggc.2017.07.019

Wassing BBT, van Wees JD, Fokker PA (2014) Coupled continuum modeling of fracture reactivation and induced seismicity during enhanced geothermal operations Geothermics 52:153-164 doi:10.1016/j.geothermics.2014.05.001

Willis-Richards J, Wallroth T (1995) Approaches to the modelling of HDR reservoirs: a review Geothermics 24:307-332

Witherspoon PA, Wang JS, Iwai K, Gale JE (1980) Validity of cubic law for fluid flow in a deformable rock fracture Water resources research 16:1016-1024

Wong LW, Blöcher G, Kastner O, Zimmermann G Multiphysics Between Deep Geothermal Water Cycle, Surface Heat Exchanger Cycle and Geothermal Power Plant Cycle. In: Comsol Conference 2012, 2012.

Xie L, Min K-B (2016) Initiation and propagation of fracture shearing during hydraulic stimulation in enhanced geothermal system Geothermics 59:107-120 doi:10.1016/j.geothermics.2015.10.012

Xie L, Min K-B, Song Y (2015) Observations of hydraulic stimulations in seven enhanced geothermal system projects Renewable Energy 79:56-65 doi:10.1016/j.renene.2014.07.044

Zeng Y-C, Su Z, Wu N-Y (2013) Numerical simulation of heat production potential from hot dry rock by water circulating through two

horizontal wells at Desert Peak geothermal field Energy 56:92−107
doi:10.1016/j.energy.2013.04.055

초   록

인공지열저류층 (Enhanced Geothemal System, EGS)에서는 수리자극을 이용해 저류층을 생성하고 투수율 향상시키는 것이 필수적이다. 균열 지열저류층에서는 기존에 존재하는 균열을 수리전단으로 팽창시켜 투수율을 향상시키는 것이 핵심적이며 수리전단으로 지속 가능한 투수율 향상을 이룰 수 있다. 균열의 유효응력변화에 따른 투수율 변화도 수리자극에서 고려되야 할 주요 수리역학적 요소이다.

본 연구에서는 포항의 균열 지열저류층 내 PX-1 과 PX-2 공의 첫 수리자극시험에서 얻어진 둘째날까지의 압력-시간 반응을 TOUGH-FLAC 시뮬레이터를 이용하여 단일 균열대 모델을 가정하여 재현하였다. PX-1 공의 모델링에서는 수리전단과 수직개구 현상이, PX-2 공 모델링에서는 수직개구현상이 고려되었다.

PX-1 모델에서는 두가지 경우의 수리적 특성에 대해 시뮬레이션이 실시되었고, 각각 첫째 날 관찰된 수리전단에 의한 압력강하와 Shut-in 이후 압력 유지를 모사하였다. 초기 이틀간의 시험에 대한 시뮬레이션 결과에서 수 백 여배의 영구적인 투수율 증가가 PX-1 공에서부터 68~110 m까지 나타났다. PX-2 모델에서는 전 기간동안 전반적으로 높은 일치도로 압력그래프가 재현되었다. 첫 2일간의 시험에 대한 시뮬레이션에서 10^{-15} m^2 대까지의 투수율 향상은 PX-2로부터 최대 15 m까지 나타났다. 본 연구는 포항 지열저류층에 대한 수치해석적 연구로서, 수리자극시험 결과의 관측 분석을 통해 예측한 각 공에서 수리자극 메커니즘을 입증하였다.

목표 유량을 위해 적합한 균열대의 투수율과 운영기간 중 생산 온도를 예측하기 위한 사전 연구가 진행되었다. 60 ℃ 의 물을 40 kg/s 의 유량으로 30년 간 순환 시키는 PX-1과 PX-2 간의 지열수 순환 모델을 만들었다. 6.74×10^{-13} m^2 ~ 6.74×10^{-12} m^2 정도의 균열 투수율에서 펌프의 압력이 35 MPa 내로 나타나며 지열수의 순환이 시뮬레이션 되었다.

주요어 : 포항 인공지열저류층, 인공지열저류층 (EGS), 수리자극, 수리역학적 모델링, 수리전단, 수직개구

학 번 : 2016-21299